

# **Philippines – Japan Joint Workshop on Materials for Safe and Sustainable Society 2012**

The University of the Philippines Diliman,  
Quezon City, Philippines  
December 6, 2012



Supported by the University of the Philippines Diliman  
and Shizuoka University

## Characterization of Water Hyacinth Fiber Treated at Different Alkali Concentration and Immersion Time

Joseph Ortenero<sup>\*</sup>, Terence Tumolva

Department of Chemical Engineering, University of the Philippines  
Diliman, Quezon City 1101, Philippines  
<sup>\*</sup>e-mail: josephortenero@gmail.com

### 1. Introduction

The use of natural fiber as reinforcement material has gained a lot of attention in recent years. This can be attributed to increase in environmental concern brought by recent environmental challenges. In addition, governments around the world introduced strict legislation to find ways in using renewable resources and reduce dependence on synthetic materials.

In natural fiber reinforced polymer (NFRP) several fibers such as jute, flax, hemp and several others have proven to be effective as reinforcement material. However, there is concern regarding production as demand for those fibers may compete with existing land devoted to food production. In this light, water hyacinth (WH) fiber could be tapped as possible substitute as this plant which is considered to be a pest in many parts of the world is excessively abundant locally. In addition, this plant has high growth rate.



Fig. 1. Water Hyacinth fiber obtained by decortication to extract the fiber from stalk.

Chemical treatment on natural fiber is necessary to improve interaction with matrix. The natural fiber undergoes surface structural and morphological changes during chemical treatment. It is this surface transformation that will play significant role in the resulting composite. In this paper, characterization of WH fiber after treatment

with NaOH was done using tensile and morphological property evaluation as well as FT-IR study.

### 2. Experimental

The NaOH used in alkali treatment was purchased from B.E. Scientific, Inc. The water hyacinth stalks were obtained at Laguna de Bay and decorticated at PTRI-DOST in Taguig.

The WH fibers were cut to 13 cm length. The fibers were soaked for 7 days to remove some lignin, waxes and any adhering dirt. The fibers were then soaked in alkali solution according to time-concentration combination of parameter. After the required immersion time the fibers were neutralized with equimolar concentration of HCl solution.

The individual fiber was then air-dried and glued on board frame for tensile property evaluation using Shimadzu AGS-X at crosshead speed of 0.5 mm/min and 25 mm gage length. Morphological property evaluation was done using Hitachi S-3400N. FTIR-ATR study was done to determine surface structural changes.

### 3. Results and Discussion

Figure 2 shows the tensile strength of the fiber at different alkali treatment period as a function of NaOH concentration. The strength of the fiber decreased as a result of the chemical treatment. The trend is as the immersion time increases tensile strength decreases except for the 24 hr immersion time. The elongation of the fiber was improved due to alkali treatment with the 10%NaOH concentration showing the highest change as exhibited in Figure 3. The stiffness of the fiber was lowered for all samples as a result of the treatment shown in

Figure 4. These changes in tensile properties of the fiber were due to removal of lignin and hemicellulose backbone. Several studies also suggest that alkali treatment leads to an increase in the amount of amorphous cellulose at the expense of crystalline cellulose<sup>1</sup>.

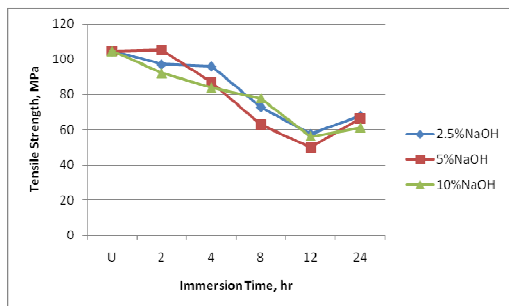


Fig. 2. Tensile strength of WH fiber at different concentration as a function of immersion time.

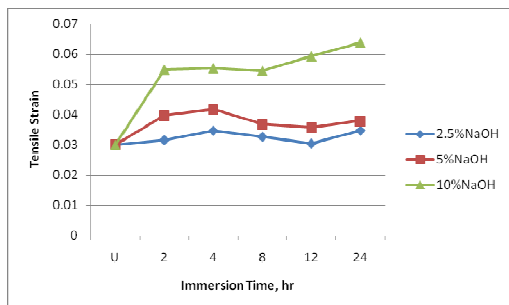


Fig. 3. Elongation at different concentration and immersion time.

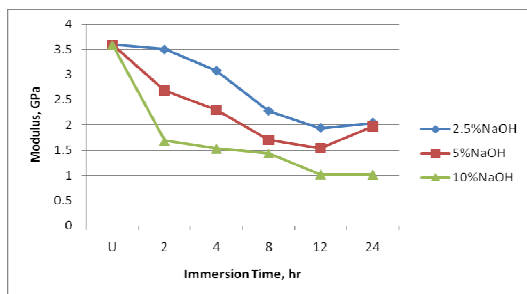


Fig. 4. Elastic modulus at different concentration and immersion time.

SEM micrographs of untreated WH fiber show significant amount of waxy natural material covering the entire surface of the fiber as presented in Figure 5(c). Also shown in the figure are images of treated WH fiber at two different concentration and immersion time. It can be observed that alkali treatment partially removed the waxy material from the surface of the fiber.

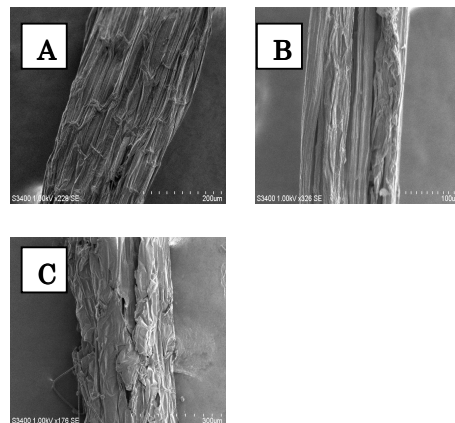


Fig. 5. SEM micrographs of WH fiber at 250x magnification. (A) 2hr & 5%NaOH, (B) 12hr & 10%NaOH, (C) untreated.

FTIR-ATR spectra for untreated WH fiber showed a broad and intense band in the range of 3100-3800  $\text{cm}^{-1}$  due to the -OH vibration of cellulose structure as shown in Fig. 6. The dip at 3400  $\text{cm}^{-1}$  decreased for treated samples. This increase in transmittance will enhance the ability of the fiber to repel moisture due to suppression of -OH group across the fiber surface.

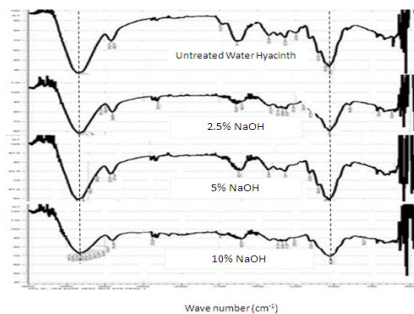


Fig. 6. FTIR-ATR spectra of treated and untreated WH fiber.

#### 4. Conclusion

Alkali treatment decreased WH fiber strength and stiffness. Morphological study revealed that alkali treatment reduced the waxy material covering the surface of the fiber. FTIR-ATR result showed reduction of -OH group across the fiber surface.

#### References

- [1] M. Mizanur Rahman, A. Mallik, M. Khan, *J. Appl. Polym. Sci.* **105** (2007), 3077-3086.
- [2] A. Gomes, K. Goda, J. Ohgi, *JSME Int. J.* **47-A** (2004), 4.

## Fatigue Property of Jute Monofilament

Kazunori UEMATSU<sup>1\*</sup>, Hideaki KATO<sup>2</sup>, Yoshinobu SHIMAMURA<sup>3</sup>, Keiichiro TOHGO<sup>3</sup> and Tomoyuki FUJII<sup>3</sup>

1 Graduate Student of Shizuoka University,  
3-5-1, Johoku, Naka-ku, Hamamatsu, 432-8561, Japan

2 Department of Mechanical Engineering, Kanagawa University,  
3-27-1, Rokkakubashi, Kanagawa-ku, Yokohama, 221-8686, Japan

3 Department of Mechanical Engineering, Shizuoka University

\*email: [kuematsu@mechmat.eng.shizuoka.ac.jp](mailto:kuematsu@mechmat.eng.shizuoka.ac.jp)

### 1. Introduction

With the increased interest in natural environments problem in recent year, green composites, which were made out of natural fibers and biodegradable plastics, are attracting attention. Green composites are applied for door-trim of automotives, cases of mobile phone and so on<sup>1</sup>. On the other hand, in order to apply for load-bearing components, unidirectional reinforcement techniques of natural fiber spun yarn have been developed to increase specific modulus and strength<sup>2,3</sup>. For applying green composites to load-bearing components, it is necessary to investigate fatigue property of green composites. In order to elucidate the fatigue property of green composites, it is necessary to clarify fatigue property of natural fibers that is a constituent of green composites. However, fatigue property of natural fiber has not been clarified. In this study the fatigue property of jute monofilament which composes jute fiber was investigated.

### 2. Materials and Specimen

#### 2.1. Structure of natural fiber

Figure 1 shows a schematic of typical natural elementary fiber. Open hole, called lumen, exists in the center of an elementary fiber. Microfibril (MF) is a bundle of cellulose, which is bonded by hydrogen bonding, surrounds around cell walls. MF has an angle to the axial direction, which determines the axial stiffness. MFs are adhered by hemicelluloses and lignin. Monofilament consists of elementary fibers that are adhered by hemicelluloses, pectin and lignin.

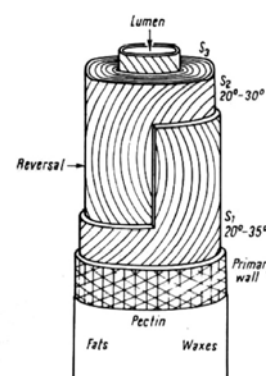


Fig.1 Structure of natural elementary

#### 2.2. Specimen

Alkaline treatment was performed for washing jute yarns. Jute monofilaments were extracted from the washed yarns. The diameter of a monofilament was measured from two perpendicular directions along the length. The cross sectional area of a fractured portion was estimated by elliptical approximation using the above data. Figure 2 shows a specimen for tensile tests and fatigue tests. According to JIS L 1069, U-shaped specimens were prepared. In fig.2, cutting line was cut after specimen was gripped.

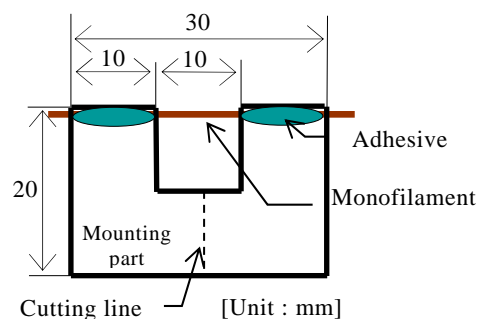


Fig.2 Specimen

### 3. Tensile test of jute monofilament

Quasi-static tensile tests were conducted to measure tensile strength. The number of specimen was 30. The cross head speed was 1mm/min and the gauge length was 10mm. Figure 3 shows the S-S diagram of jute monofilament and Table 1 shows the mechanical properties. Tensile strength and Young's modulus of jute monofilament have a scatter as shown in fig.3. Therefore, it is necessary to consider this scatter when the fatigue property of jute monofilament is discussed.

Table 1 Mechanical properties of jute monofilament

	Tensile strength		Young's modulus	
	Average	S.D.	Average	S.D.
Jute	149MPa	147MPa	16GPa	5GPa

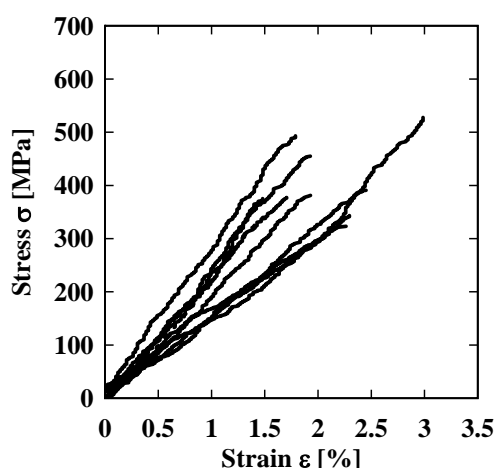


Fig.3 S-S diagram of jute monofilaments

### 4. Fatigue test of jute monofilament

Fatigue testing was conducted at room temperature. Loading frequency was 10Hz and the gauge length was 10mm. The stress ratio is 0.1 and the maximum stress was 60 to 120% of the tensile strength.

Figure 4 shows the S-N diagram. The error bar at 1 cycle is the standard deviation of the tensile strength.

Fatigue strength at  $10^6$  cycles was about 50% of the tensile strength. Therefore, fatigue property of jute monofilaments seems to be superior. Figure 5 shows the fracture portion after fatigue testing. Splitting among elementary fibers and pull out of secondary wall in an elementary fiber were found.

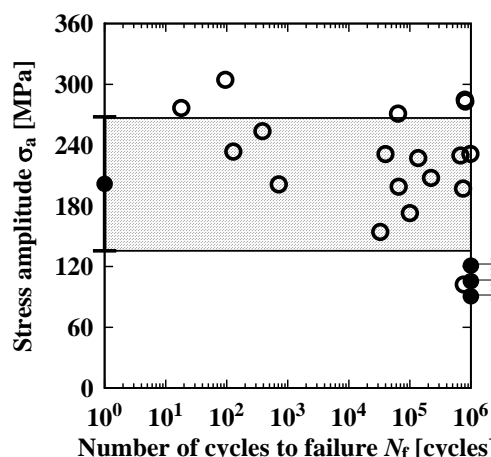


Fig.4 S-N diagram of jute monofilaments

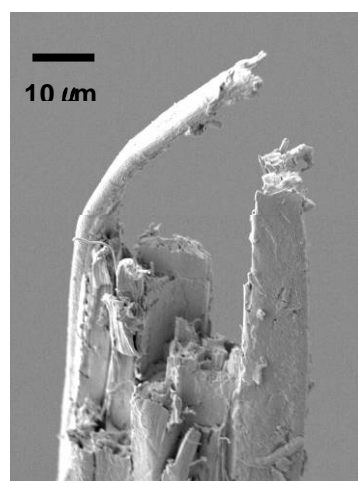


Fig.5 Jute monofilament after fatigue

### 5. Conclusions

- (1) The fatigue property of jute monofilament seems to be superior.
- (2) Splitting between elementary fibers and pull out of secondary wall were found after fatigue failure.

### Reference

1. F.P.L.Mantia, M.Morrela, Composites Part A, Vol.42, No.6 (2011), pp.579-588.
2. O.A.Khondker, U.S.Ishikua, A.Nakai and H.Hamada, Composites Part A, Vol.37, No12, (2006), pp.2274-2284
3. G.Ben, Y.Kihara, K.Nakamori and Y.Aoki, Advanced Composite Materials, Vol.16, No. 4, (2007), pp.361-376.
4. M.A.Meyers, P.Y.Chen, A.Y.M.Lin, Y.Seki, Progress in Materials Science, Vol.53, No.1, (2008), pp.152-206

## Microencapsulated Coconut Oil as a Buffering PCM for Textile Applications

Hyacinth Mae G. Tambago\*, Thor Alexis S. Sazon, Gilbert S. Casuyon,  
Al Christopher C. de Leon, Rizalinda L. de Leon

Department of Chemical Engineering, Melchor Hall, University of the Philippines,  
Diliman, Quezon City 1101, Philippines  
TEL: +63-2-981-8500 loc 3114 TEL&FAX: +63-2-929-6640  
\*e-mail: [hyacinth\\_mae.tambago@up.edu.ph](mailto:hyacinth_mae.tambago@up.edu.ph)

### 1. Introduction

Phase change materials (PCMs) are thermal energy storage substances that have high latent heats of fusion. During melting or solidification, these substances can store or release large amounts of energy with temperatures maintained constant at their melting point. Due to this property, PCMs can be incorporated in window textile and composites to serve as a thermal barrier, reducing energy consumption for cooling of spaces against solar heat. For such applications, encapsulation of the PCM is necessary to contain the material in its liquid phase and prevent material losses due to evaporation. When particles are contained in solid, polymeric shells of 1-1000 micrometers in diameter, the process is called microencapsulation. Microencapsulated PCMs exhibit improved heat transfer and cycling stability due to smaller size and higher surface-to-volume ratio.

One advantage of microencapsulation is that it allows PCMs to be incorporated in textile, which requires the size of the particles to be in the range of 3-10  $\mu\text{m}$ . PCM content of microcapsules for this application is 80-85% by volume and the polymeric shell is around 1  $\mu\text{m}$  thick [1].

Coconut oil is a relatively cheap and abundant natural material in the Philippines that can function as a buffering PCM. With a melting temperature of 25-27°C slightly lower than ambient temperature during the day, and high latent heat of fusion of 54-126 J/g [2], coconut oil can aid air-conditioners in thermal regulation of cooled spaces. In this study, microcapsules of coconut oil as PCM were synthesized via in-situ polymerization using melamine and

formaldehyde as shell materials and sodium dodecyl sulfate (SDS) surfactant as emulsifier. Thermal properties of the microencapsulated coconut oil particles were measured and the surfactant concentration was investigated for its effect on PCM content, particle size, and mechanical strength. Based on these properties, the potential of the synthesized microencapsulated coconut oil for textile applications was evaluated.

### 2. Experimental

The oil/water emulsion was prepared by mixing coconut oil, water, and SDS using a homogenizer. Two SDS concentrations were used: 1.25% and 3% SDS. Melamine, formaldehyde, and water were mixed under basic conditions in creating the pre-polymer solution, which was then added into the emulsion. The resulting mixture was continuously homogenized and then cooled, filtered, and dried to obtain the microcapsules.

The chemical structure of coconut oil and microencapsulated coconut oil were determined using a Shimadzu Prestige 21 FTIR spectrophotometer. Thermal properties of the microcapsules were measured using a Shimadzu DSC-50. Particle sizes were measured from optical microscopy images and the mechanical strength of the microcapsules was qualitatively evaluated using a centrifugal shear force test.

### 3. Results and Discussion

The FTIR spectra of coconut oil and the synthesized microcapsules are shown in Fig. 1. With respect to the spectra of pure coconut oil, the appearance of a broad band in the 3703-3036

$\text{cm}^{-1}$  region and peaks at 814, 1520, 2931, and 1469, and 1173  $\text{cm}^{-1}$  in the spectra of the microcapsules correspond to melamine and formaldehyde chemical groups and the chemical linkages that result from polymerization. This indicates formation of melamine-formaldehyde polymer and successful encapsulation of coconut oil.

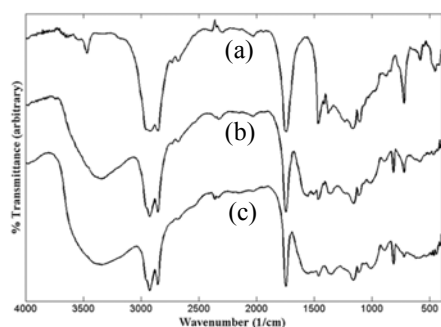


Fig. 1. FTIR spectra of a) pure coconut oil, b) microcapsules with 1.25% SDS, and c) microcapsules with 3% SDS.

Thermal properties of microcapsules synthesized from 1.25% and 3% SDS derived from DSC thermograms are tabulated in Table 1. The average peak melting point of the microcapsules is 24.61°C, which is within the range of comfort temperature. Microcapsules prepared from 3% SDS emulsion exhibited higher latent heat of fusion compared to that with 1.25%. This also indicates that microcapsules prepared using a higher surfactant concentration contain a larger amount of coconut oil per unit mass.

Table 1. Thermal and physical properties of microencapsulated coconut oil.

	Microcapsules from	
	1.25% SDS	3% SDS
Melting temperature, °C	24.55	24.67
Heat of fusion, J/g	23.15	44.69
Mean particle diameter, $\mu\text{m}$	27.87	11.15
Particle diameter range, $\mu\text{m}$	11.00-55.98	3.43-19.73

The mean particle diameters and size range of the microcapsules are also tabulated in Table 1. Surfactant concentration of 3% in the emulsion yielded smaller particles with a narrower size distribution than those formed by using 1.25% SDS. In the centrifugal shear force test, microcapsules prepared from 3% SDS

exhibited lower mechanical strength, as evidenced by an oil leak from the microcapsules. This could be due to formation of rough surfaces at higher surfactant concentrations, resulting in microcapsules with reduced mechanical strength [3].

Although the microcapsules synthesized from the 3% SDS emulsion resulted in smaller particles, they are still not sufficiently small for textile applications. The PCM content could not be determined without the latent heat of fusion of pure coconut oil and imaging of an open microcapsule is required to determine the thickness of the polymeric shell.

#### 4. Conclusion

Coconut oil has been successfully encapsulated by melamine-formaldehyde polymer. The microencapsulated coconut oil exhibited a melting point within our comfort zone. Higher surfactant concentration in the oil-water emulsion resulted in smaller and more homogeneously sized particles with higher coconut oil content but with lower mechanical strength. In order to satisfy requirements for textile applications, synthesis of much smaller microencapsulated coconut oil particles with higher mechanical strength should be explored. Further tests such as characterization of pure coconut oil, thermal cycling stability and morphological analysis of microcapsules, and thermal and durability analysis of fabrics treated with microencapsulated PCM should be conducted in order to fully characterize the potential of microencapsulated coconut oil for this application.

#### References

- [1] M. V. Parys (2006). Smart Textiles using Microencapsulation Technology. In S. K. Ghosh, *Functional Coatings by Polymer Microencapsulation* (pp. 221-258). Weinheim: WILEY-VCH Verlag GmbH & Co. KGaA.
- [2] A. Rudd, *ASHRAE Transactions* **99** (1993) 339-346.
- [3] H. Zhang & X. Wang, *Colloids and Surfaces A: Physicochemical and Engineering Aspects* **332**, (2009) 129-138.

## Stress Corrosion Crack Initiation in Austenitic Stainless Steel under High-Temperature and Pure Water Environment

Yutaro Miura<sup>1</sup>, Akihiro Kenmochi<sup>2</sup>  
 Tomoyuki Fujii<sup>3</sup>, Keiichiro Tohgo<sup>3</sup> and Yoshinobu Shimamura<sup>3</sup>  
<sup>1</sup>Under graduate student of Shizuoka University  
<sup>2</sup>Graduate student of Shizuoka University  
<sup>3</sup>Department of Mechanical Engineering, Shizuoka University,  
 3-5-1Johoku, Naka-ku, Hamamatsu 432-8561, Japan  
<sup>a</sup>ymiura@mechmat.eng.shizuoka.ac.jp

### 1. Instruction

Stress corrosion cracking (SCC) is an inherently complicated material degradation phenomenon induced by certain combinations of material, environment, and stress condition. It has been reported that SCC occurs under the corrosive conditions in chemical plants and nuclear power plants. It is important to clarify the crack initiation and propagation behavior by SCC under the corrosive conditions from the viewpoint of remaining lives in long-term service.

In this paper, the constant tensile load tests under High-Temperature and Pure Water Environment, this is equal to simulated primary water environment in a boiling water reactor (BWR) were carried out for sensitized stainless steel to investigate influence of applied load and loading time on crack initiation propagation behavior by SCC.

### 2. Material and Experiment

#### 2.1 Material and Specimen

Austenitic stainless steel type 304 was used. The stainless steel was sensitized by heat treatment in order to accelerate crack initiation by SCC. Table 1 shows the chemical composition of the material.

Figure 1 shows the geometry of the specimen. The specimens were machined from the bulk material after the heat treatment and their surfaces were polished and buff-finished. The specimen has three different cross-section parts in order to load different level of stresses at a time. In order to accelerate crack initiation by SCC, the crevice was formed on the specimen surface by using graphite fiber wool (GFW).

Table1. Chemical composition of SUS304

C	Si	Mn	P	S	Ni	Cr	Fe
0.06	0.47	0.82	0.03	0.003	8.05	18.16	Bal

#### 2.3 Experimental environment

The constant tensile load tests under simulated primary water of boiling water reactor are carried out. Table 2 shows the test conditions.

At first, the specimens were pre-immersed in 48 hours. After that, the load was applied. After the experiments, the specimens were etched by 10% oxalic acid to remove oxide film and expose grain boundary on the specimen surface. The number of cracks and maximum crack length were measured by using an optical microscope and scanning electron microscope (SEM) in order to evaluate the influence of the applied load and loading time on the crack initiation and coalescence behavior by SCC.

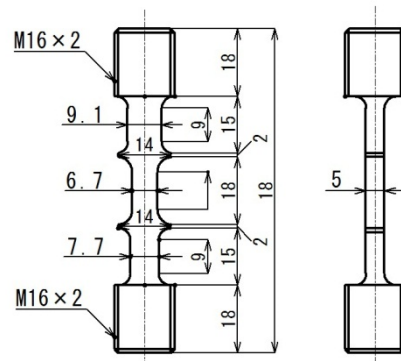


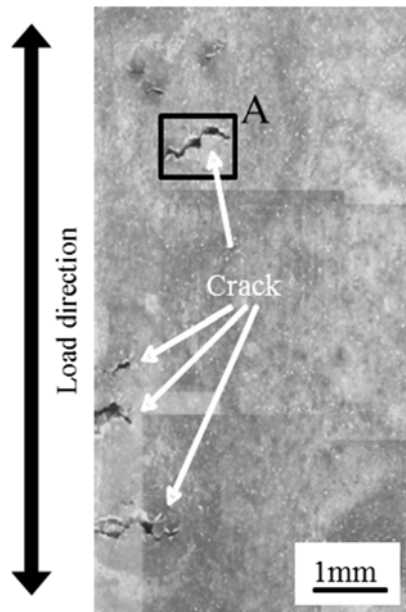
Fig.1. Shape of specimen

Table2. Test condition

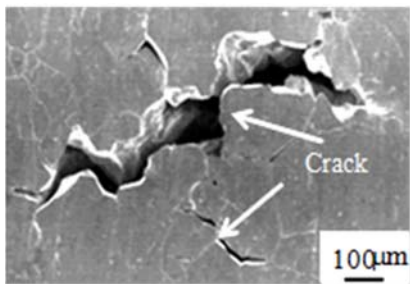
Temperature	288°C
Pressure	8MPa
Conductivity	0.1µS
Dissolved oxygen concentration	8ppm
Stress levels	175MPa 210MPa 250MPa

### 3. Experimental results

Figure 2 shows surface observation under the applied load of 250MPa for 120hours. Figure 2(a) is overall view of the specimen surface, and Fig. 2(b) is the magnified views of part A in Fig.2 (a). Many cracks at normal direction to loading direction are observed in Fig.2 (a). The stress corrosion cracks initiated at the grain boundary in Fig. 2(b).



(a) Over all veiw



(b) Detail of A

Fig.2.Cracks on specimen surface (120hr,250MPa)

Figure 3 shows the number of cracks as a function of loading time. The error bars denote the maximum and minimum number of cracks. The number of cracks increases with increasing loading time and applied load.

Figure 4 shows the histogram of the frequency of cracks as a function of crack length less than 100µm when the applied stress is 250MPa. The most frequent crack is about 60µm in length when the crack is less than 100µm. The frequency curves between the crack length and the number of crack is bell-shaped. Therefore, it seems that the probability of the crack initiation by SCC is normal-distributed. The mean value of the normal-distribution is 52µm and the variance is 15µm, irrespective of applied load.

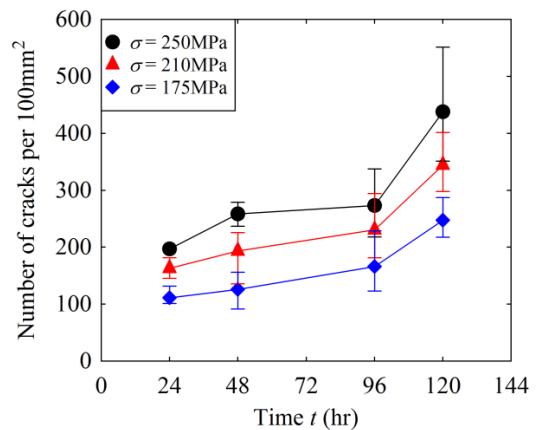


Fig.4. Number of cracks as a function of time.

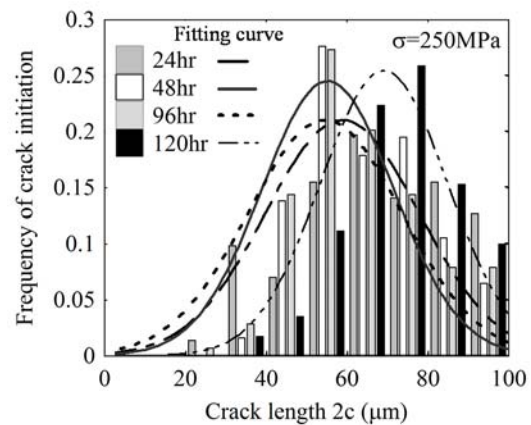


Fig.6. Histogram of number of cracks as a function of crack length under 100µm (250MPa).

### 4. Conclusion

- (1) The number of cracks and maximum crack length increases with increasing loading immersion time and applied load.
- (2) The probability of the crack initiation by SCC is normal-distributed. The mean and variance are constant irrespective of applied load.

## Synthesis of Furfural from Locally Available Agricultural Residues in the Philippines

Rodel D. Guerrero<sup>a\*</sup>, Emmanuel P. Belostrino<sup>a</sup>, Mark Louis H. Lagura<sup>a</sup>, Billy Joe Y. Uy<sup>a</sup>,  
Terence P. Tumolva<sup>a</sup> and Masatoshi Kubuoichi<sup>b</sup>

<sup>a</sup>Department of Chemical Engineering, University of the Philippines,  
Diliman 1101 Quezon City, Philippines  
TELEFAX: +6329296640

<sup>b</sup>Department of Chemical Engineering, Tokyo Institute of Technology,  
2-12-1 O-Okayama Meguro-ku, Tokyo, 152-8552 Japan  
\*email: [rodeldayaguerrero@gmail.com](mailto:rodeldayaguerrero@gmail.com)

### 1. Introduction

Furfural, with an IUPAC systematic name of 2-furancarboxaldehyde and molecular structure is a clear and colorless oily liquid with a benzaldehyde-like odor. Furfural has an array of uses thus it is now widely used in large quantities as a solvent, to accelerate vulcanization, as an ingredient to production of phenolic resins and many more.

In producing furfural, materials rich in pentosans are used. Pentosan is found in hemicellulosic fibers like bagasse, hulls, nut shells, corn cobs and oats. After extraction, pentosan is converted to furfural.

The Philippines produces a myriad of agricultural products. The country capitalizes on its fertile lands and its tropical climate to support a thriving agricultural industry. Of the 30 million hectares of land in the country, 40% is agricultural. It also shows that the Philippines main agricultural crops are sugarcane, which accounts the largest production volume, followed by palay, coconut, banana and corn.

Given the data and the top agricultural products of the country, it is possible to deduce the most viable option for raw materials in producing furfural. It follows that the crops with the highest production volume generate the highest amounts of waste, hence making them good candidates for raw materials.

With those in mind, finding locally available raw materials for the production of furfural, the important intermediate for the production of furfuryl alcohol, could prove to be beneficial. The recognition of new alternatives could increase the feasibility of

commercialization of furfural. The full utilization of our agricultural residues, by turning them into sources for plastic production and other applications, could greatly help in boosting the economy. Also, making the manufacturing process more adapted to the Philippine setting can attract investors and companies to construct a furfural plant in the Philippines. And lastly, the Philippines can satisfy our demand in furfural and could also become a major supplier of furfural in the world market.

Thus, this paper proposes locally available raw materials that have not been previously used in furfural production. Based on the agricultural crops production data in the country, the raw materials chosen are coconut shell, coconut husk, pineapple bagasse, and water hyacinth stalks.

### 2. Experimental

#### Materials

The raw materials used were coconut shell, coconut husk, pineapple bagasse and water hyacinth stalks.



Figure 1. The raw materials used in the study.

### Synthesis of furfural

A pulverized air-dried sample of the raw material (0.100 g) was placed inside a 10 mL glass test tube. Dilute sulfuric acid (0.2 M) solution of 3.5 mL in volume was then pipetted to the test tube and covered with a cap. The test tube was immersed in an oil bath and was heated for the specified digestion period (10, 15, 20 minutes) at 453 K. at the end of the digestion time, the test tube was cooled promptly by being immersed in a water-cooled bath. The test tube was opened and the product was filtered out and washed with hot water to a 50 mL beaker. The furfural was precipitated with the addition of 20 mL 2,4-dinitrophenylhydrazine solution (2,4 DNPH). The precipitate was then filtered and first washed with 2 M HCl solution and followed by washing with distilled water. The precipitate yield of furfural 2,4-dinitrophenylhydrazine is quantitative (Demirbas, 2006) (Kazemi et. al., 2009).

### 3. Results and Discussion

Tables 1 and 2 show the average mass yield and standard deviations for each raw material at different digestion times:

Raw Material	Mass Yield		
	10 mins	15 mins	20 mins
Coconut Husk	4.3069	5.5132	5.546
Coconut Shell	6.2729	6.9262	7.2108
Pineapple Bagasse	3.5941	4.9989	5.5208
Water Hyacinth	2.6067	2.6888	3.6369

Table 1. Average mass yields.

Raw Material	Standard Deviation		
	10 mins	15 mins	20 mins
Coconut Husk	0.7769	1.2971	0.7451
Coconut Shell	0.9444	0.7466	0.7783
Pineapple Bagasse	1.1675	0.656	0.4015
Water Hyacinth	1.8986	0.2778	1.3339

Table 2. Average standard deviations.

Coconut shell gave the highest mass yield with 7.21%, followed by coconut husk with 5.55%, pineapple bagasse with 5.52%, and finally water hyacinth with 3.64%. The deviations in the values of the mass yields at the same hydrolysis time may be attributed to the fluctuations in the temperature of the

oil bath and the possible escape of furfural vapor from the reaction tubes.

Figure 2 shows that the values of the mass yield increase with increasing hydrolysis time.

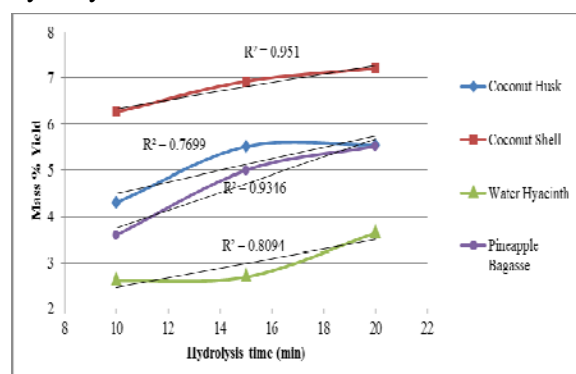


Figure 2. Mass yield as a function of hydrolysis time (T = 180 deg Celsius)

Coconut shell gave the highest  $R^2$  value which indicates that it is the most sensitive to changes in hydrolysis time. Increasing the hydrolysis time further will give higher mass yields.

### 4. Conclusion

The proposed experimental design was found to be successful in the synthesis of furfural. The method used is also significantly simpler and more practical than other existing methods found in several literatures. The coconut shells were observed to have the highest furfural yield among the chosen raw materials. The furfural yield was also observed to have a general trend of increasing yield with increasing hydrolysis time for all raw materials with coconut shells being the most sensitive to the changes in hydrolysis time.

### Reference

- [1] Demirbas, Ayhan. "Furfural Production from Fruit Shells by Acid-Catalyzed Hydrolysis." Energy Sources, Pat A. (2006): 11.
- [2] Kazemi, M., Zand-Monfared, M.R., "Furfural Production from Pistachio Green Hulls as Agricultural Residues." Journal of Applied Chemical Researches (2009): 19-24.
- [3] Hitchcock, R.L., Froneberg, B., "Commercial Production of Furfural in its Twenty-fifth Year," Chemical Engineering Progress, 44 (1984): 669-674.

## Influence of tension during cure on tensile property of carbon nanotube spun yarn reinforced epoxy

Kahori Oshima<sup>1</sup>, Yoshinobu Shimamura<sup>1</sup>, Keiichiro Tohgo<sup>1</sup>,  
Tomoyuki Fujii<sup>1</sup>, and Yoku Inoue<sup>2</sup>

<sup>1</sup>Department of Mechanical Engineering, Shizuoka University,  
3-5-1 Johoku Naka-ku, Hamamatsu, 432-8011, Japan

<sup>2</sup>Department of Electrical and Electronic Engineering, Shizuoka University

### 1. Introduction

Carbon nanotubes (CNTs) are expected to exceed the mechanical properties of conventional carbon fibers, but growing continuous CNTs has limitation so far. Consequently, it is difficult to apply CNTs to structural components. In order to solve this matter, spinning of CNTs has been investigated, and continuous fibers of CNT spun yarn can be fabricated easily [1]. In addition, CNT composite made out of CNT spun yarn are expected to be applicable to structural components. However, the basic mechanical properties of CNT spun yarn reinforced composite have not been clarified.

In this study, CNT spun yarn reinforced epoxy was fabricated by using the pultrusion technique, and influence of tension during cure on tensile property of CNT composite was examined.

### 2. Materials

Multi walled carbon nanotube (MWNT) spun yarn was used as reinforcement. MWNT used in this study was grown on a quartz glass plate with chemical vapor deposition using  $C_2H_2$  and  $FeCl_2$  as a base material and a catalyst, respectively [1]. The MWNT length was around 1 mm and the diameter was 50 nm. The spun yarn diameter was about  $45 \mu m$  and the twist angle  $\alpha$  was between  $27\sim 35^\circ$ .

Bisphenol-A type room-temperature curing epoxy (Bisphenol-A type) was used as matrix of MWNT composite.

### 3. Fabrication of MWNT composite

MWNT composites were fabricated by using the pultrusion technique. Figure 1 shows a schematic of pultrusion process of MWNT composites. A die ( $\phi 120 \mu m$ ) was

made in a plastic plate for the pultrusion. A MWNT bundle was dipped into resin and then pultruded through the die. Then, a dead weight was attached to the bottom of the bundle while curing. Four different weights from 10 g to 30 g were used in this study.

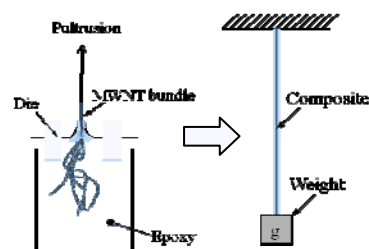


Fig.1 Pultrusion process of MWNT spun yarn reinforced composite

### 4. Influence of tension during cure

Tensile tests of MWNT composite were conducted at room temperature. The cross head speed was 1mm/min and the gauge length was 15 mm. Strain was measured by using a non-contact extensometer.

Figure 2 shows the relationship between volume fraction of fiber and weight. The volume fraction increased with increasing weight. This is because resin in MWNT spun yarns was squeezed out by applying tensile force.

Figure 3 shows tensile properties of MWNT composite with the volume fraction of fiber. Young's modulus and tensile strength improved with increasing the volume fraction. The maximum Young's modulus was 53 GPa, and the maximum tensile strength was 485 MPa. The higher tensile properties were probably brought by better load transfer to MWNT because of the high aspect ratio of MWNT.

## 6. Conclusions

1. The pultrusion technique of spun yarn was effective in improving volume fraction and fiber orientation of MWNT composite.
2. Tensile properties of MWNT composite were improved by tension during cure because of the increase of volume fraction and fiber orientation.
3. The fracture surface of MWNT composite implies that fracture mode of MWNT composite was fiber breakage.

## Reference

- [1] Y. Inoue, K. Kakihata, Y. Hirono, T. Horie, A. Ishida, and H. Mimura, *APPLIED PHYSICS LETTERS*, 92 (2008), 213113

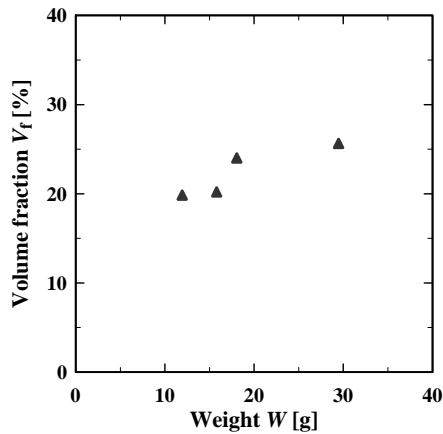


Fig.2 Volume fraction vs. weight

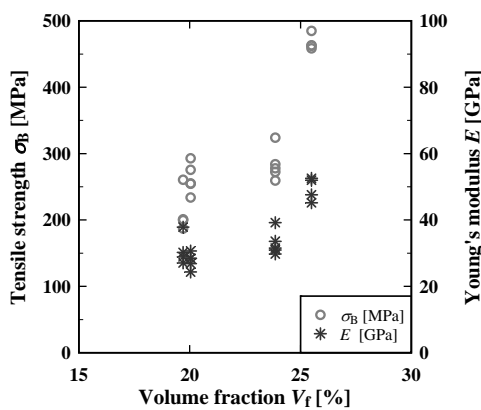


Fig.3 Tensile properties vs. volume fraction

## 5. Fracture surface

Figure 4 shows a typical fracture surface of MWNT composite ( $W=29.5g$ ,  $\sigma_B=458MPa$ ). MWNT pull-out length was about  $10 \mu m$  while MWNT length was 1 mm. The result implies that fracture mode of MWNT composite was fiber breakage.

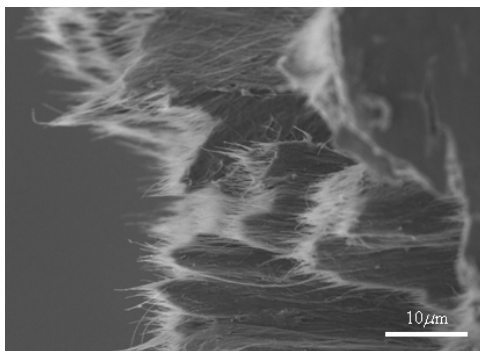


Fig.4 Fracture surface of composite ( $W=29.5g$ ,  $\sigma_B=458MPa$ )

## Particle Size Distribution and Iron Loading of Iron Oxide-Coated Sand Sorbent

Jay R T. Adolacion\*, and Maria Lourdes P. Dalida

Department of Chemical Engineering, College of Engineering, University of the Philippines,  
Diliman, Quezon City, Philippines

TEL&FAX: +63-2-929-6640

\*e-mail: jayr.adolacion@coe.upd.edu.ph

### 1. Introduction

Iron-oxide coated media has been used as sorbents in the removal of various water pollutants. These granular materials are characterized by an ensemble of different particles sizes which may have varying amounts of iron oxide coated unto it. In the study of these particulate sorbents, one of the parameters affecting its sorption kinetics is the sorbent dosage, which is the ratio between the mass of sorbent and the amount of sorbate solution. In the absence of *in-situ* methods for obtaining kinetic data, the alternative is to carry out *ex-situ* studies, normally involving withdrawal of aliquots. However, it will not be possible to maintain constant sorbate dosage in the process. This in turn will influence the quality of the kinetic data that can be obtained.

The problem is further compounded by the effect of scale on the sorbate dosage. Small-scale sorption studies are prone to variability inherent in small granular sorbent samples. In the case of iron oxide-coated media, variability arises from variations in particle size distribution, and possibly, variations in the loading of iron-oxide sorbent on the surface of the supporting media (Fig. 1).

Thus, in order to quantify the effects of aliquot withdrawal on kinetic measurements, it is necessary to first determine the range of sample sizes where variations in particle size distribution and iron-oxide loading become insensitive to sample size.

In this study, the variations in the particle size distribution and iron loading were compared across different quantities of iron oxide-coated sand (IOCS) samples. The iron loading was taken as a measure of the amount of iron oxide present on the IOCS surface. The results were subjected to statistical tests to determine any significant

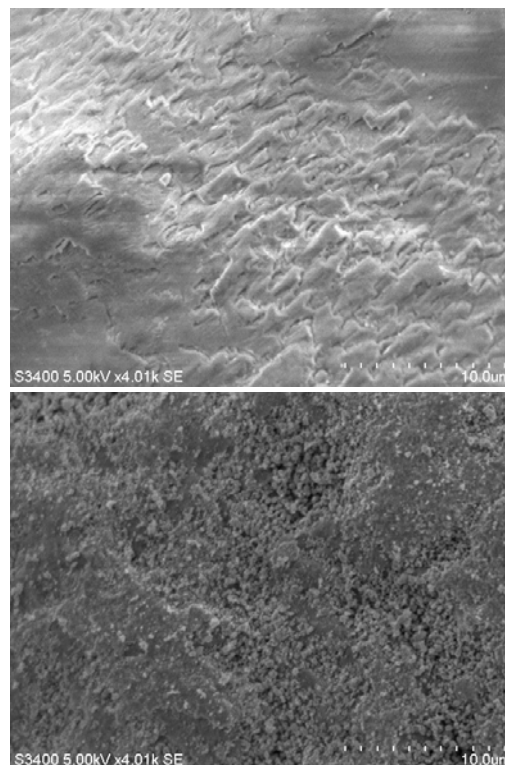


Fig. 1. SEM images of silica sand before (top) and after (bottom) coating with iron oxide. The rough surface after coating is due to the iron-oxide deposited on the sand surface, concentrated mostly on cavities.

difference in the means and variances between samples.

### 2. Particle Size Distribution and Iron Loading Measurements

Pretreated white beach sand was coated with iron oxide using the method by Li *et al.* [1]. Iron oxide sand samples were obtained by tumble mixing prior to scoop sampling. Image scans from several samples were taken to obtain estimates for the population and sample particle size distributions (Fig. 2).



Fig. 2. An image scan of iron oxide-coated sand (IOCS). Millimeter marks are shown on the lower left.

The particle size distributions were obtained using digital image analysis via *ImageJ* software [2]. IOCS samples were dissolved in strong acid and the resulting solutions were analyzed for their iron content using HR-CS AAS.

### 3. Results and Discussion

The particle size distributions were observed to converge at higher sample weights starting at 50-mg IOCS. The variability in iron loading decreased with increasing sample weight; however, larger sample quantities were accompanied by the appearance of outliers. F-tests suggest that variances became insensitive to sample size at 50 mg and above while T-tests suggest that mean values seem to be the same at 25 mg and higher in both the particle size distribution and iron loading measurements. Translation of the results to particle count suggests a minimum value 260 IOCS particles to minimize variability attributable to the granular nature of the IOCS. For adsorption studies, it may be recommended to fix the amount of adsorbent and vary the quantity of solution instead when using small quantities of adsorbent.

### 4. Conclusion

Variability inherent in granular sorbents may be lessened by using a sufficiently large enough quantity of sample. Consequently, variability in sorbent dosage can be minimized by fixing the amount of sorbent and adjusting the amount of the sorbate solution instead in order to achieve the desired dosage.

### References

- [1] Li Dongmei, Huang Hui, Ye Tingjin, Huang Mingzhu, Ren Yi, Liu Chunliu, He Na, International Conference on Computer Distributed Control and Intelligent Environmental Monitoring. (2011) 1823-1826.
- [2] WS Rasband, U. S. National Institutes of Health. (1997-2011)

## Stress Analysis of Spun Yarn Reinforced Composites

Diyun Miao<sup>1</sup>, Yoshinobu Shimamura<sup>2</sup>, Keiichiro Togo<sup>2</sup>, and Tomoyuki Fujii<sup>2</sup>

<sup>1</sup>Undergraduate Student, Shizuoka University, Japan

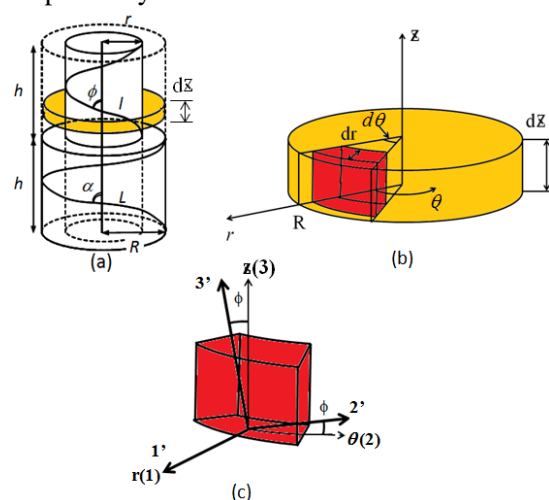
<sup>2</sup>Department of Mechanical Engineering, Shizuoka University, Japan  
1-7-29 Nunohashi, Naka-ku, Hamamatsu, Shizuoka 432-8012, Japan  
e-mail: dmiao@mechmat.eng.shizuoka.ac.jp

### 1. Introduction

Staple spun yarns are used as preform for natural fiber reinforced composites for decades. In addition, innovative techniques to make spun yarn from carbon nanotubes have recently emerged; this will enable us to make carbon nanotube reinforced composites more easily. A spun yarn has very complex geometry of staple fibers such as twist, migration and discontinuity. The complexity gives rise to difficulty for analyzing staple spun yarn. Thus, analyzing staple spun yarn reinforced composites is a challenge but necessary for developing the new types of composite materials.

### 2. Stress analysis by using theory of elasticity

A model shown in Fig.1 is used to analyze staple spun yarn reinforced composites. Displacements in of the  $r, \theta$  and  $z$  directions are represented as  $u, v$  and  $w$ , respectively.



(a) Helical reinforcement, (b) An element in composite, (c) Definition of coordinates

Fig.1 Microelement in a cylindrical coordinate system.

The following assumptions are adopted in this study:

- axially symmetric deformation,
- no torsion around the  $z$ -axis, and
- uniform strain along the  $z$ -axis direction.

Thus, displacements in the  $r, \theta$  and  $z$  directions are expressed as

$$u = u(r), v = 0, w = w(z) \quad (1)$$

### 2.1 Strain-displacement relations

Substituting Eq.(1) into generalized strain-displacement relations for a cylindrical coordinates gives the following equations.

$$\epsilon_r = \frac{\partial u}{\partial r}, \quad \epsilon_\theta = \frac{1}{r} \frac{\partial v}{\partial \theta} + \frac{u}{r} = \frac{u}{r},$$

$$\epsilon_z = \frac{\partial w}{\partial z} = \epsilon_z^0,$$

$$\gamma_{r\theta} = \gamma_{\theta z} = \gamma_{zr} = 0 \quad (2)$$

### 2.2 Constitutive equation

A coordinate system  $1'2'3'$  shown in Fig.1(c) is defined as a material coordinate system. Filaments are aligned in the  $3'$  axis.

The compliance matrix  $C'$  in the material coordinate system is written as

$$C' = \begin{bmatrix} 1/E_r & -\nu_{rr}/E_r & -\nu_{LT}/E_L & 0 & 0 & 0 \\ & 1/E_r & -\nu_{LT}/E_L & 0 & 0 & 0 \\ & & 1/E_L & 0 & 0 & 0 \\ & & & 1/G_{LT} & 0 & 0 \\ Sym & & & & 1/G_{LT} & 0 \\ & & & & & 2(1+\nu_{TT})/E_r \end{bmatrix} \quad (3)$$

$E_L, E_T, \nu_{TL}$  and  $\nu_{TT}$  can be calculated by using the rule of mixture and the shear-lag model.

Relationships between stress and strain components in the reference and material coordinate systems are described as

$$\sigma' = T_\sigma \cdot \sigma, \quad \epsilon' = T_\epsilon \cdot \epsilon \quad (4)$$

where  $T_\sigma$  and  $T_\epsilon$  are rotation matrices. By using the Eq.(4), a stiffness matrix  $D$  is expressed as

$$D = C^{-1} = T_\sigma^{-1}(C')^{-1} \cdot T_\epsilon \quad (5)$$

In this case,

$$\tau_{\theta z} = 0, \quad \tau_{zr} = 0 \quad (6)$$

but  $\tau_{r\theta}$  is not always zero in order to present torsion around the z-axis.

### 2.3 Equilibrium equations

Force equilibriums in the  $\theta$  and  $z$  directions always hold from Eq.(6). The force equilibrium in the  $r$  direction is expressed as

$$\frac{\partial \sigma_r}{\partial r} + \frac{\sigma_r - \sigma_\theta}{r} = 0 \quad (7)$$

### 2.4 Governing equation

From Eqs.(2), (5) and (7), the governing equation is derived.

$$\frac{\partial}{\partial r} \left( d_{11} \frac{\partial u}{\partial r} + d_{12} \frac{u}{r} + d_{13} \epsilon_z^0 \right) + \frac{1}{r} \left\{ (d_{11} - d_{21}) \frac{\partial u}{\partial r} + (d_{12} - d_{22}) \frac{u}{r} + (d_{13} - d_{23}) \epsilon_z^0 \right\} = 0 \quad (8)$$

The differential equation of Eq.(8) can be solved under the following boundary conditions.

$$u(0) = 0, \quad \sigma_r(R) = 0 \quad (9)$$

### 2.5 Young's modulus of staple spun yarn reinforced composites

Young's modulus of a staple spun yarn reinforced composite can be calculated as follows.

At first, the total force  $P$  in the z-axis direction is

$$P = \int_0^R \int_0^{2\pi} \sigma_z \cdot dr \cdot (rd\theta) = 2\pi \int_0^R \sigma_z \cdot r dr \quad (10)$$

Then, the average stress and Young's modulus of the composite are given as

$$\bar{\sigma} = \frac{P}{A} = \frac{P}{\pi R^2} = \frac{2}{R^2} \int_0^R \sigma_z \cdot r dr,$$

$$E = \frac{\bar{\sigma}}{\epsilon_z^0} \quad (11)$$

## 3. Example

Young's modulus of jute fiber-reinforced polymer with a twisting angle  $\alpha$  is calculated by using the mathematical model. The physical properties of a jute fiber-reinforced polymer are shown in Table1.

Table1 Physical properties

Material	Jute
Radius of fiber [m]	$6.0 \times 10^{-5}$
Length of fiber [m]	$6.0 \times 10^{-4}$
Volume fraction of fiber [%]	45
Young's modulus of fiber [GPa]	27.4
Young's modulus of resin [GPa]	0.8
Poisson's ratio of fiber [-]	0.3
Poisson's ratio of resin [-]	0.3

Figure 3 shows Young's modulus of jute fiber-reinforced composites as a function of the twisting angle  $\alpha$ .

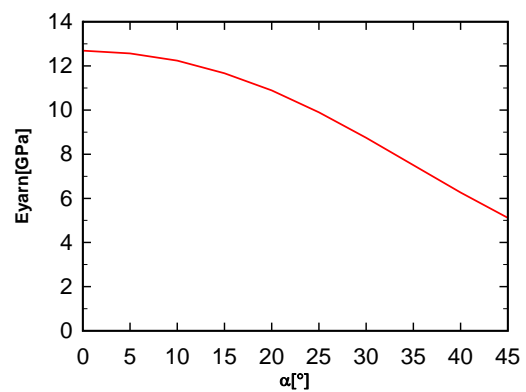


Fig.3 Young's modulus of Jute spun yarn reinforced composite.

## 4. Conclusions

An analytical method for spun yarn reinforced composites based on the theory of elasticity was proposed and an example was demonstrated.

## Comparison of Various Dip-Coated and Spray-Coated TiO<sub>2</sub> Catalysts for Photocatalytic Reactor Applications

Patrick D. Ramoso\*, Maria Lourdes P. Dalida

Department of Chemical Engineering, College of Engineering, University of the Philippines,  
Diliman, Quezon City 1101, Philippines  
TEL&FAX: +63-2-929-6640  
\*e-mail: pdramoso@up.edu.ph

### 1. Introduction

Pollution from industrial effluents continues to be a threat to our water supplies. With this, the challenge of developing an efficient wastewater treatment process has been studied in the past years. Photocatalysis has been extensively studied for its ability to completely mineralize organic and inorganic contaminants from water [1]. Many organic pollutants in water can be completely decomposed at the surface of UV-irradiated TiO<sub>2</sub>; these include alkanes, haloalkanes, aliphatic alcohols, carboxylic acids, alkenes, aromatics, haloaromatics, polymers, surfactants, herbicides, pesticides and dyes [2].

The photocatalytic reaction is initiated by the excitation of TiO<sub>2</sub> by UV light having energies greater than or equal to the band gap energy, resulting to the generation of mobile electrons and positive holes. This starts a chain of reactions leading to the complete mineralization of organics to carbon dioxide and water. The photocatalyst could either be suspended in a slurry or immobilized on a support. Slurry systems require a post-process separation such as filtration to separate the catalyst. In an immobilized system, the operation is continuous and it does not need any additional separation process. However, it may be vulnerable to catalyst wash out [3].

In this study, Degussa P25 TiO<sub>2</sub> photocatalyst was immobilized on glass using various coating methods. The supported catalysts were subjected to scanning electron microscopy (SEM) for surface characterization.

### 2. Experimental

Degussa P25 TiO<sub>2</sub> (25% rutile, 75%

anatase) was used as the photocatalyst to be coated on glass. Two glass materials were used to support the catalyst: 1) glass Raschig rings approximately ¼ inch in diameter; 2) modified tubular reactor of approximately 12 inches in length. Various coating methods listed in Table 1 were used to immobilize the TiO<sub>2</sub>.

Table 1. Coating methods

Method	Description
1	TiO <sub>2</sub> -water slurry on Raschig rings by dip-coating
2	TiO <sub>2</sub> -ethanol slurry on Raschig rings by spray-coating
3	TiO <sub>2</sub> -ethanol slurry on tubular reactor by air-assisted spray-coating

The first method discussed in Table 1 served as reference to a previous study on TiO<sub>2</sub> coating on glass Raschig rings [4]. For method 2, the dip-coating method was replaced by spray coating using an atomizer. Method 3 used compressed air to coat the catalyst on a modified glass tubular reactor.

The glass-supported catalysts were allowed to stand and dry for 24 hours, and were calcined afterwards at 573 K. SEM images of the calcined catalyst were obtained using a Hitachi S-3400N scanning electron microscope.

### 3. Results and Discussion

Figures 1 to 3 show the resulting SEM images of the calcined catalysts prepared using methods 1 to 3, respectively.

The dip-coated TiO<sub>2</sub>-water slurry on glass Raschig rings in Figure 1 shows a non-uniform dispersion of the catalyst on the glass surface. Aside from this, multiple layers of TiO<sub>2</sub> are observed; this is not a

desired characteristic of immobilized catalysts due to unutilized catalyst surface.

The spray-coated TiO<sub>2</sub>-ethanol slurry on glass Raschig rings as shown in Figure 2 indicates complete surface coverage of the glass surface with TiO<sub>2</sub>. The layering of catalyst is relatively even, but the problem of multilayer coating is still quite evident.

The air-assisted spray coating of TiO<sub>2</sub>-ethanol slurry on a glass tubular reactor, seen in Figure 3, shows complete surface coverage with a less degree of multilayer coating. This may have been caused by the compressed air, which could have improved the dispersion of the TiO<sub>2</sub>-ethanol slurry as it is sprayed onto the glass surface. The length of the tubular reactor may have also contributed to a more even coating since any excess slurry would just flow to adjacent areas within the reactor, in contrast to spray-coating on glass rings, at which the slurry tends to accumulate on the glass rings, causing multilayer coating.

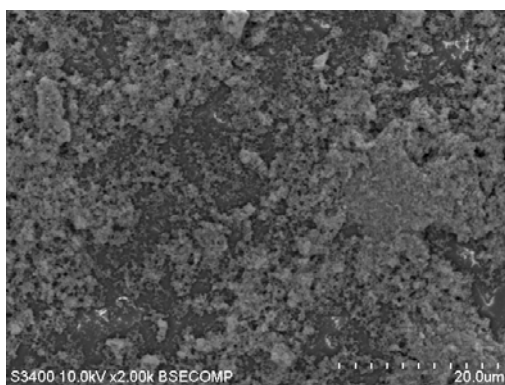


Fig. 1. SEM image of TiO<sub>2</sub> dip-coated on glass Raschig rings

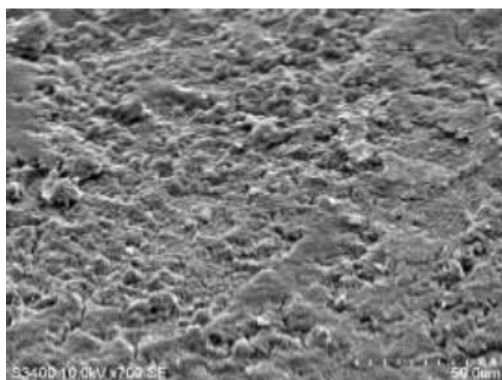


Fig. 2. SEM image of TiO<sub>2</sub> spray-coated on glass Raschig rings

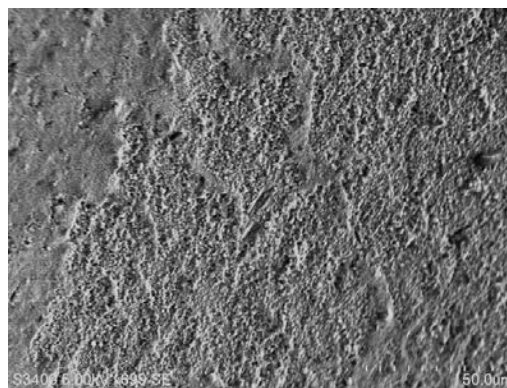


Fig. 3. SEM image of TiO<sub>2</sub> spray-coated on glass tubular reactor

#### 4. Conclusion

Air-assisted spray coating on long glass tubular reactors provided the most uniform dispersion of TiO<sub>2</sub> photocatalyst among the various methods tested. It is recommended to proceed with this method in performing actual runs to mineralize organic substances.

#### Acknowledgments

The authors thank Angella Rainbow Lim, Karmina Grace Bautista and Riuji Sato for the fabrication and TiO<sub>2</sub>-spray coating of the tubular photocatalytic reactor, and Adolph Bravo Jr., Ervin Cezar and Darlene Que for the preparation of TiO<sub>2</sub>-coated Raschig rings.

#### References

- [1] K. Nagaveni, G. Sivalingam, M.S. Hegde and G. Madras, *Appl. Catal. B. Environ. Lett.* **48** (2004) 83-93.
- [2] A. Fujishima, X. Zhang and D.A. Tryk, *Surf. Sci. Rep.* **63** (2008) 515-582.
- [3] H. de Lasa, B. Serrano and M. Saldaña, 2005. *Photocatalytic Reaction Engineering*. USA: SpringerLink.
- [4] P. Ramoso, M.P. Dalida. (2011). *Dip coating of TiO<sub>2</sub> photocatalyst on glass raschig rings for flow photocatalytic reactor application*. Presented in: Japan-Philippine Joint Workshop on Materials for Safe and Sustainable Society 2011. Hamamatsu, Japan.

## Diffusion of Inorganic Acids in Epoxy and Polyurethane Thermosetting Resins

Jonas Karl Christopher N. Agutaya<sup>a\*</sup>, Zarlou M. Bernardo<sup>a</sup>, Lorenz Anthony T. Fernando<sup>a</sup>,  
Timothy David T. Salmo<sup>a</sup>, Terence P. Tumolva<sup>a</sup>

<sup>a</sup>Department of Chemical Engineering  
University of the Philippines, Diliman, Quezon City 1101 Philippines  
TEL&FAX: +632-929-6640  
Email: [jnagutaya@gmail.com](mailto:jnagutaya@gmail.com)

### 1. Introduction

Chemical recycling is the conversion of waste polymers into feedstock or fuels (Lin & Yang, 2009). Various efforts of plastics recycling were made in the past decade. However, recycling of thermosets like epoxies and polyurethane displays a unique problem due to its network structure of cross-linking chains.

Epoxies commonly used today are diglycidyl ether of bisphenol-A (DGEBA), which is a product between epichlorohydrin and bisphenol A (Anon., n.d.). These epoxies are commonly used in manufacturing coatings, adhesives and glass fiber reinforced plastics (GFRP).

On the other hand, polyurethane is a product of a reaction between a diisocyanate and a polyol. The common uses of polyurethanes are in the manufacturing of rigid foams used in refrigeration and roof and wall insulations, coatings, and other sports equipment and furniture.

Most applications of these thermosets are for long-term purposes due to their cross-linked chains, which give durability. However, the cross-linked chains also make it difficult for this type of plastic to be recycled.

In this study, the rate of diffusion – as a precursor to dissolution – of inorganic acid in epoxy and polyurethane was compared qualitatively. The acids used were H<sub>2</sub>SO<sub>4</sub>, HNO<sub>3</sub> and HCl, and the temperatures were 30°C, 50°C, and 80°C.

### 2. Methodology

#### 2.1. Preparation of Resins and Acids

Epoxy and polyurethane thermosetting resins were purchased from *Polymer Products Philippines, Inc.* Both polymers were moulded into 2 cm × 4 cm × 2 mm sheets. Each sheet was weighed prior to immersion in acid.

From the stock solutions purchased from local suppliers, 5M solutions of sulfuric acid, nitric acid, and hydrochloric acid were prepared.

#### 2.2. Decomposition experiments

Each specimen was immersed in 150 mL of a particular acid in a beaker. Each beaker was then placed in oil baths at 30°C, 50°C, and 80°C. Three sets of five specimens were prepared for each acid at a particular temperature.

Over a period of 12 days, samples were periodically taken out of the beaker and were weighed using an analytical balance. The percentage of weight loss was then plotted against the square root of time. Plateau points were identified.

### 3. Results and Discussions

#### 3.1. Change in weight of epoxy resin

**Figure 1** shows that the mass of the epoxy resin increased continuously at 30°C for all the acids. At this temperature, the diffusion process was more prevalent than the reaction of the acid with the epoxy.

In the case of the immersion of epoxy in HCl and H<sub>2</sub>SO<sub>4</sub> solutions at 50°C, the same trend of increasing mass was also apparent. However, in the case where HNO<sub>3</sub> was used as the acid, a more abrupt increase in mass of the resin occurred after 36 hours. After 210 hours, the mass of the resin continuously decreased until the resin dissolved completely.

The trends at 50°C can also be observed at 80°C. However, the reaction between HNO<sub>3</sub> and epoxy at this temperature is more prevalent than at 50°C as evidenced by an actual decrease in weight of the epoxy resin with respect to its original mass. The resin completely dissolved in the acid after 72 hours.

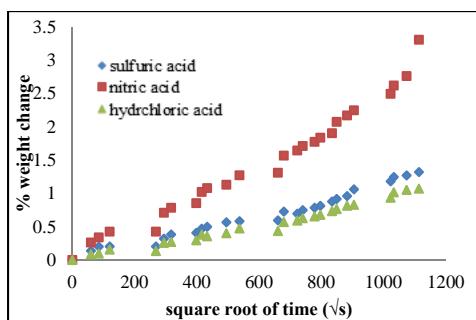


**Figure 1.** Percentage weight gain of epoxy resin vs. square root of time at 30°C.

### 3.2. Change in weight of polyurethane resin

The mass of the polyurethane resin at 30°C increased then stabilized (**Figure 2**). There was a more rapid increase in the weight of the polyurethane resin as compared to the epoxy. This is mainly due to a porous structure (Forrest, 1999) of the polyurethane. Also, the percent change of the PU resin in HNO<sub>3</sub> is thrice as much as compared to the resins submerged in the H<sub>2</sub>SO<sub>4</sub> and HCl. The increase in weight of the resin in HNO<sub>3</sub> is attributed to the formation of a tertiary amine salt group upon reaction (Abacha, et al., 2009).

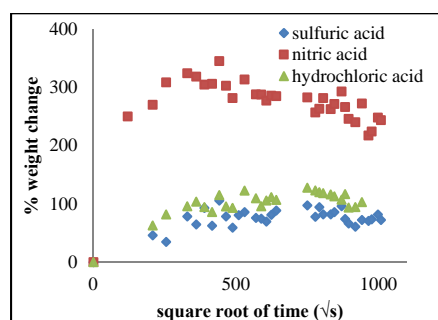


**Figure 4.** Percentage weight gain of polyurethane resin vs. square root of time at 30°C.

The previous trend in HNO<sub>3</sub> also manifested at 50°C. At this temperature, the HCl also exhibited the trend similar to HNO<sub>3</sub>. The percent change in weight for both acids was close to 300%. This observation is consistent according to the general reaction of polyurethane resin with an inorganic acid, which produces amine salt (Behrendt & Naber, 2009). However, after 156 hours, the PU resin in HNO<sub>3</sub> and HCl significantly decreased in mass.

The trend for the previous temperatures was the same for 80°C. Resin continued to increase in weight due to the formation of the amine salts. After 156 hours,

the resin dissolves into the solution. The data gathered for the PU resin submerged in HNO<sub>3</sub> is limited for 12 hours since beyond that point, the resin is very brittle, hence, very difficult to subject to analysis.

## 4. Conclusion

For the epoxy resin, nitric acid diffuses the fastest, followed by sulfuric acid, then hydrochloric acid. On the other hand, nitric acid diffuses in polyurethane the fastest, followed by hydrochloric acid, and lastly, sulfuric acid.

Furthermore, an increase in temperature improves the diffusion in both polymers for all the acids.

## References

### Journals

1. N. Abacha, M. Kubouchi, T. Sakai, K. Tsuda (2009). Diffusion behavior of water and sulfuric acid in epoxy/organoclay nanocomposites. *Journal of Applied Polymer Science*, **112**: 1021-1029.
2. G. Behrendt, B. W. Naber (2009). The chemical recycling of polyurethanes (review). *Journal of the University of Chemical Technology and Metallurgy*, **44**: 3-23.
3. Y.-H. Lin, M.-H. Yang (2009). Kinetic and mechanistic modeling of acid-catalyzed degradation of polymers with various cracking catalysts. *Journal of Applied Polymer Science*. **114**: 2591-2599.

### Book and book chapter

1. M. Forrest (1999). *Chemical Characterisation of Polyurethanes*, United Kingdom: Rapra Technology Ltd..

### Internet

1. Anon. (n.d.). Chemistry of Epoxies / Epoxy Resin, Novolacs. Available from <http://www.epoxyproducts.com/chemistry.html>. Accessed August 2011.

## Upgrading functionalities of Ultrasonic Torsion Fatigue Testing Machine

Akito KOKUBO<sup>1\*</sup>, Yoshinobu SHIMAMURA<sup>1</sup>, Hiroki MASUDA<sup>1</sup>,  
Hitoshi ISHII<sup>2</sup>, Keiichiro TOHGO<sup>1</sup>, Tomoyuki FUJII<sup>1</sup>, Tooru YAGASAKI<sup>3</sup>  
and Masamichi HARADA<sup>3</sup>

<sup>1</sup> Department of Mechanical Engineering, Shizuoka University  
3-5-1 Johoku, Naka-ku, Hamamatsu, Shizuoka 432-8561, Japan

<sup>2</sup>Professor Emeritus, Shizuoka University

<sup>3</sup>Honda R&D Co., Ltd

\*e-mail: akokubo@mechmat.eng.shizuoka.ac.jp

### 1. Introduction

Recently, fatigue failure due to gigacycle loading (more than  $10^7$  cycles) has been reported. It is necessary to investigate gigacycle fatigue. However, the loading frequencies of conventional fatigue testing machines are around 20Hz. It takes 19 months to achieve gigacycle if the frequency is 20 Hz.

For reducing the testing time, we have developed an ultrasonic torsional fatigue testing machine. The cyclic frequency of the testing machine is around 20 kHz. It takes only 14 hours to achieve gigacycle and this machine enables us to accelerate fatigue testing considerably. In this study, we developed a new ultrasonic torsion fatigue testing machine in order to solve difficulties of the existing testing machine. In addition, fatigue tests were conducted by using the new testing machine to confirm the performance.

### 2. New Ultrasonic Torsion Fatigue Testing Machine

#### 2.1 Ultrasonic torsion fatigue testing machine

Configuration of an ultrasonic torsion fatigue testing machine is shown in Fig.1. The main components of the ultrasonic torsion fatigue testing machine are a signal generator, a torsional oscillator, an amplifying horn and a specimen. A signal generator generates electronic signal at the resonance frequency of the horn and specimen. Torsional oscillator converts the electronic signal into a torsional displacement at the same frequency. Thus

cyclic loading can be applied to the specimen due to resonance. Since the torsional displacement generated by the oscillator is small, the torsional displacement is amplified by decreasing the sectional areas of horn and specimen.

#### 2.2 Features of new testing machine

New testing machine adopts a signal generator that can automatically tune the resonance frequency and can be controlled through external input; fatigue tests can be controlled by using a PC.

In an existing testing machine, torsional displacement amplitude depend on mass of a specimen. On the other hand, in the new testing machine, displacement amplitude was almost constant regardless of specimen's mass because we adopted a well-tuned amplifier.

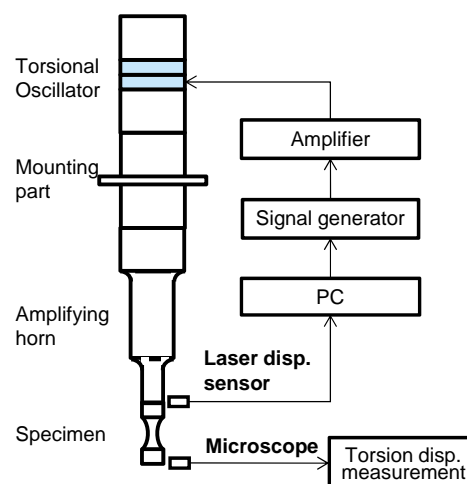
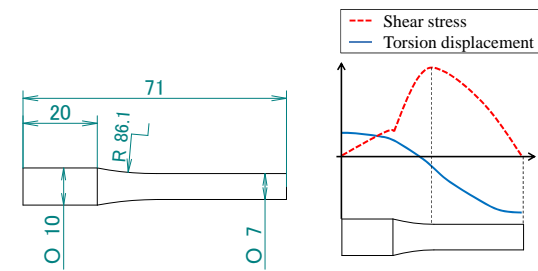


Fig. 1 Ultrasonic torsion fatigue testing machine.

### 3. Material and specimen

Alloy steel (SCM420H) was used in this study. The shape and shear stress distribution in a specimen are presented in Fig.2. Specimen was annealed, quenched and then tempered. The conditions of the heat treatment are presented in Table.1.



(a) Specimen shape (b) Shear stress distribution  
Fig. 2 Specimen.

Table 1 Heat treatment condition.

	Heat up		Soaking		Temperature fall
	Temperature [°C]	Time [min]	Temperature [°C]	Time [min]	
Annealing	900	60	900	40	Furnace cooling
Quenching	900	30	900	45	Oil cooling
Tempering	180	10	180	120	Air cooling

### 4. Fatigue tests

Ultrasonic torsion fatigue tests were conducted for the specimens. The stress ratio R was -1, and loading frequency was about 20 kHz. When the reduction of the resonance frequency was more than 30Hz, fatigue tests were interrupted. Since heat generation was remarkable during test, intermittent loading were set to suppress temperature increase within an allowable range (i.e. less than 100°C in the case of steel). The maximum shear stress was estimated from a torsional displacement at the end of a specimen using a relationship between them obtained by FEM analysis. The torsional displacement was measured using a microscope during fatigue testing.

An S-N diagram was plotted in Fig. 3. The fatigue strength at  $10^9$  cycles was about 170MPa. The surface of a failed specimen at  $1.4 \times 10^8$  cycles was observed. A star shaped crack was found as shown in Fig.4.

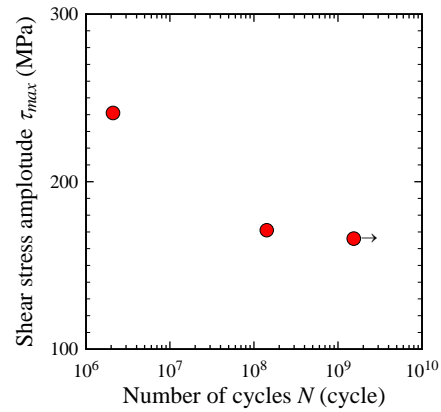


Fig. 3 S-N diagram.

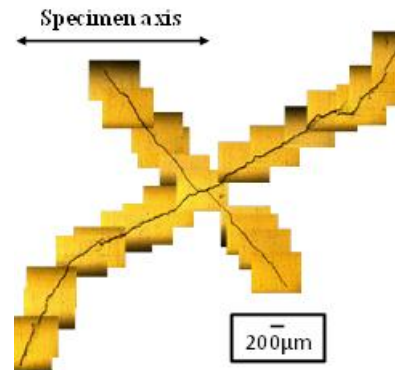


Fig. 4 Fatigue crack ( $N_f = 1.4 \times 10^8$ )

### 5. Conclusions

A new ultrasonic torsion fatigue testing machine was developed and fatigue tests by using this testing machine were conducted. Fatigue strength at  $10^9$  cycles of quenched and tempered SCM420H was about 170MPa. A star shaped fatigue crack was observed for the failed specimen.

## A Degradation Study for the Acid Recycling of Polyurethane and Polyfurfuryl Alcohol Resins

Ronald P. Bual<sup>1,2</sup>, Terence P. Tumolva<sup>1</sup>

<sup>1</sup>Department of Chemical Engineering, University of the Philippines – Diliman Quezon City 1101 Philippines, <sup>2</sup>Department of Chemical Eng'g. & Tech., MSU-Iligan Institute of Technology, Iligan City 9200 Philippines,

<sup>1</sup>e-mail: [rpb0853@gmail.com](mailto:rpb0853@gmail.com)

### 1. Introduction

Concern for the environment, both in terms of limiting the use of finite resources and the need to manage waste disposal, has led to increasing pressure to recycle waste materials. Ever since the first industrial scale production of synthetic polymers took place, the production, consumption and waste generation rate of plastic has increased significantly. Thus, recycling of plastic wastes has been a focus of many researches in the past few decades.

Enormous efforts have been launched in the field of disposal of plastic wastes in recent years, especially thermosetting resin that is difficult to recycle due to its network structure of cross-linking chains. Chemical recycling is a new and promising technique for converting plastic wastes by returning them back to its original constituents, that is, monomers or petrochemical feedstock, and has received a great deal of attention in recent years [1].

In this study, the chemical recycling of two thermosetting resins was conducted; polyurethane (PU) and polyfurfuryl alcohol (PFA) resins. This study will further investigate the effect of two parameters in the degradation of the resins. These parameters are the type of strong inorganic acids (HCl, H<sub>2</sub>SO<sub>4</sub>, HNO<sub>3</sub>) used as the solvent and the immersion temperature. The study will be extended to the diffusion of acid in polyurethane resin as well. The diffusion reaction mechanisms were studied given varying temperature with the goal to establish parametric data that will help further researches on chemical recycling.

### 2. Methodology

#### 2.1. Materials and sample preparation

PU resin was purchased from *Polymer Products Philippines, Inc.* in set A & B. The components were mixed in a 1:1 ratio. Then it was allowed to harden in personally designed plastic containers for hours and was cut into 2cm x 4cm x 2mm. Meanwhile, PFA resin was provided by *Hitachi Chemical Co., Ltd.*, cured and was cut into the desired dimension. Then the weights of the samples were taken before immersing them into the acids.

#### 2.2 Degradation Experiment

Eighteen beakers were used for the set-up; each was filled with 150 mL of acids. The samples were then submerged into the acids, with the top part of the sample hanging into modified clips. The beakers were then sealed with plastic wrap, and placed according to their maintaining temperature. Thermostat waterbaths, that were purchased from *BE Scientific Glass Instruments*, were used to maintain the three temperatures.

#### 2.3 Weighing

After a certain time interval, mostly at a six hour period, samples were taken out of the beaker, then dampened into tissue papers and were weighed using an analytical balance.

#### 2.4 Analytical Methods

From the mass weighing data, percent weight change versus square root of time was plotted to investigate the effect of the parameters considered. FT-IR will be used to analyze chemical reactions. GCMS, DSC, SEM will also be used to characterize the virgin and recycled resin.

### 3. Results and Discussion

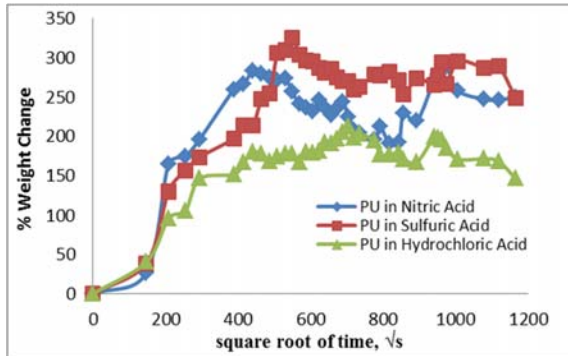


**Figure 1.** Percentage weight change of PU vs. square root of time at 30 °C in three different acids.

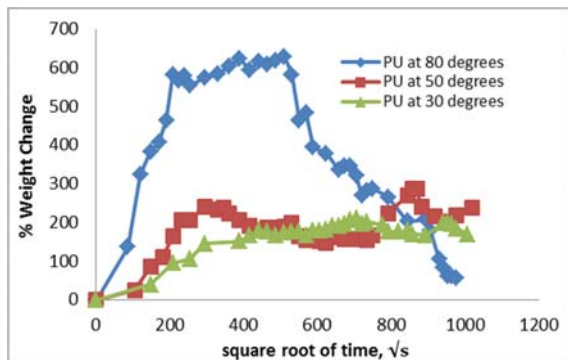


**Figure 2.** Percentage weight change of PU vs. square root of time in hydrochloric acid at various temperatures.

Figure 1 and Figure 3 shows the effect of the three strong inorganic acids to polyurethane and polyfurfuryl alcohol at 30 °C. While Figure 3 and Figure 4 shows the effect of three different temperatures in hydrochloric acid. It can be implied from the trends that diffusion is more prevalent in the reaction of the PU resin than the reaction of the PFA resin with the acid.

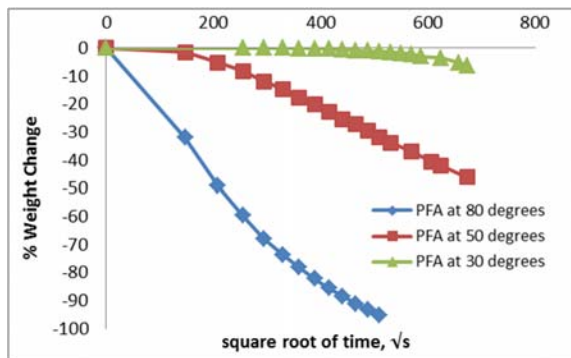


**Figure 3.** Percentage weight change of PFA vs. square root of time at 30 °C in three different acids.

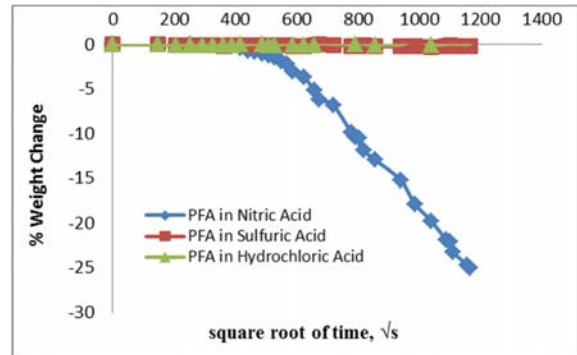


**Figure 4.** Percentage weight change of PFA vs. square root of time in nitric acid at various temperatures.

The mass of the PU resin at 30 °C increases then stabilizes. This trend proves that the mass of the resin is already close to its maximum weight. The effect of temperature is seen in Figure 2 with the percent weight change of PU resin increased as high as 600% and decreased continuously at 80 °C. This shows that diffusion and degradation proceeds at a faster rate when the temperature is high.

In Figure 3 and Figure 4, the degradation of PFA resin is faster with nitric acid than the other acids.

### 4. Conclusion

The change of weight (%) of the thermoset resin is proportional to temperature and varies greatly with the type of inorganic acid used.

Diffusion of the acid takes place first for PU, followed by the side reactions which further increase the weight of the resin, then followed by the breakage of the polyurethane group. While the degradation of PFA resin proceeds via breakage of the cross-linking bond.

It could be said that among the three acids HNO<sub>3</sub> is the fastest to diffuse and degrade the polymer. And among the three temperatures, 80°C makes the reaction proceed fast as compared to the two.

### Reference

[1] Dang, W., Kubouchi, M., Sembokuya, H., & Tsuda, K. (2005). *Chemical recycling of glass fiber reinforced epoxy resin cured with amine. Polymer* 46, 1905–1912.

## Effect of Specimen Size on the Gigacycle Torsion Fatigue Properties

Takanori IZUMIKAWA<sup>1\*</sup>, Yoshinobu SHIMAMURA<sup>1</sup>, Hiroki MASUDA<sup>1</sup>,  
Hitoshi ISHII<sup>2</sup>, Keiichiro TOHGO<sup>1</sup>, Tomoyuki FUJII<sup>1</sup>, Tooru YAGASAKI<sup>3</sup>  
and Masamichi HARADA<sup>3</sup>

<sup>1</sup> Department of Mechanical Engineering, Shizuoka University  
3-5-1 Johoku, Naka-ku, Hamamatsu, Shizuoka 432-8561, Japan

<sup>2</sup>Professor Emeritus, Shizuoka University

<sup>3</sup>Honda R&D Co., Ltd

\*E-mail: tizumikawa@mechmat.eng.shizuoka.ac.jp

### 1. Introduction

Recently, fatigue failure due to gigacycle loading (more than  $10^7$  cycles) has been reported. It is necessary to investigate gigacycle fatigue. Since the loading frequencies of conventional fatigue testing machines are around 20Hz, it takes 19 months to achieve gigacycle. Therefore, developing a new method that can accelerate fatigue testing is required, and ultrasonic torsional fatigue testing machines have been developed. The cyclic frequencies of ultrasonic testing machines are around 20 kHz. It takes only 14 hours to achieve gigacycle and it is possible to reduce fatigue testing time considerably. However, research on the frequency effect and size effect on fatigue life is limited. In general, fatigue strength obtained by ultrasonic torsion fatigue testing are higher than that of conventional methods.

In this study, fatigue testing was conducted for two types of specimens with different risk volumes by using an ultrasonic torsion fatigue testing machine, and the effect of specimen size on gigacycle torsion fatigue property of high strength steel was investigated.

### 2. Ultrasonic Torsion Fatigue Testing Machine

The configuration of an ultrasonic torsion fatigue testing machine used in this study is shown in Fig.1. The main components of the ultrasonic torsion fatigue testing machine are a signal generator, a torsional oscillator, an amplifying horn and a specimen. A signal generator gives electronic signal at the resonance frequency of the horn

and specimen. Torsional oscillator converts the electronic signal into a torsional displacement at the same frequency. Thus cyclic loading can be applied to the specimen due to resonance. Since the torsional displacement generated by the oscillator is small, the torsional displacement is amplified by decreasing the sectional areas of horn and specimen.

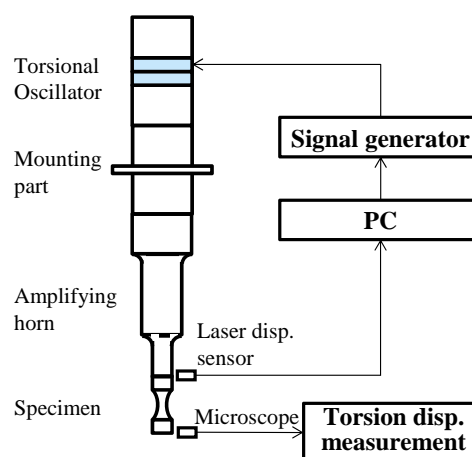


Fig. 1 Ultrasonic torsion fatigue testing machine.

### 3. Size effect and frequency effect

The size effect on torsion fatigue properties using conventional and ultrasonic torsion fatigue testing machines was studied by Sakanaka [1]. Figure 2 shows the result. Open diamonds are torsion fatigue testing results of large specimens with  $318.9\text{mm}^3$  risk volume. Open circles are torsion fatigue testing results of small specimens with  $3.570\text{mm}^3$  risk volume, and solid circles are results of small specimens with  $3.126\text{mm}^3$  risk volume by using ultrasonic torsion

fatigue testing. As shown in Fig.2, the risk volume has significant effect on the fatigue strength as well as frequency. This is called size effect. Size effect is brought from increase of the existence probability of critical defects such as non-metal inclusions.

### 5. Conclusion

Two types of specimens with different risk volumes were designed successfully and are now under fatigue testing.

### Reference

[1] N. Sakanaka, Y. Matsubara, Proceedings of JAST Tribology Conference, 2012, 257-258.

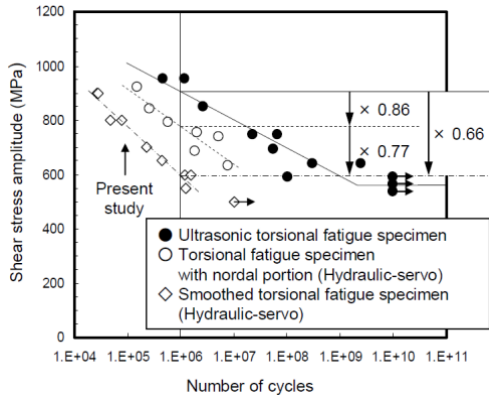


Fig. 2 S-N diagrams obtained by torsional fatigue tests [1]

### 4. Design of specimens

Two types of specimens with a large risk volume and a small risk volume were designed. Basic dimensions were determined by using a theoretical formula, but FEM analysis was also performed to tune the torsion resonance frequency (20kHz). Figure 3 shows dimensions of specimens and shear stress distributions. An Hourglass shape specimen shown in Fig.3 (a) has a small risk volume of 4.88mm<sup>3</sup> because shear stress distribution profile is sharp. On the other hand, a half dumbbell shape specimen shown in Fig.3 (b) has a large risk volume of 56.5mm<sup>3</sup> (11.6 times greater than that of the hourglass shape specimen) because shear stress distribution profile is moderate.

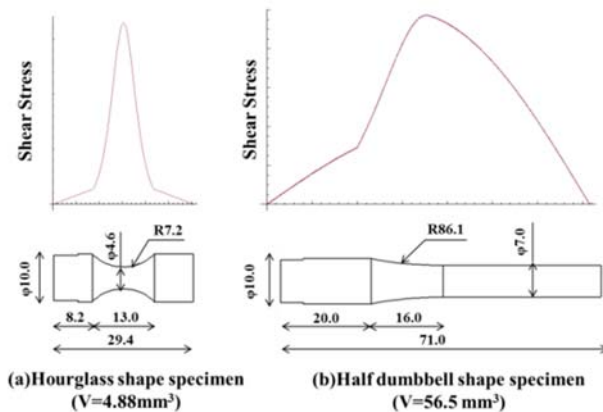


Fig. 3 Dimensions of specimens and shear stress distribution. .

## Lifetime Prediction of Furan Resin using Thermal Analysis

Jhud Mikhail O. Aberilla<sup>a\*</sup>, Terence P. Tumolva<sup>a</sup>, and Masatoshi Kubouchi<sup>b</sup>

<sup>a</sup> Department of Chemical Engineering  
University of the Philippines, Diliman, Quezon City 1101 Philippines

<sup>b</sup> Department of Chemical Engineering  
Tokyo Institute of Technology, Meguro-ku, Tokyo 152-8552 Japan

\*Corresponding Author's E-mail: joaberilla@up.edu.ph

### 1. Introduction

At present, there is already a great abundance of research on natural fiber reinforced polymeric (NFRP) composites- mostly on the evaluation and improvement of mechanical performance when using non-biodegradable composite matrices such as thermosetting resins. However, limited data is available to gauge the environmental advantages of these materials- in particular, the carbon storage potential with the use of renewable bio-based materials. Since CO<sub>2</sub> fixation capacity is the key environmental parameter evaluated in this study, certain LCA principles are applied on the material to serve as a guide and tool for the evaluation of carbon storage potential. For long-term CO<sub>2</sub> fixation, the bio-based carbon content of a material is just one of the parameters that must be determined in order to evaluate overall carbon storage potential- another parameter that must be considered is the lifetime of the material.

Due to the long lifetime of highly stable furan (>10<sup>2</sup> years), it is definitely not feasible to simply wait and directly measure the longevity of carbon fixation of the resin and its composites; therefore, a different approach is necessary. One popularly known method of predicting lifetime of polymeric materials is by thermogravimetric analysis (TGA). In this study, TGA is performed to evaluate the thermal decomposition of furan by measuring the weight loss at a fixed heating rate, and the parameters of the degradation kinetics are obtained to establish lifetime.

### 2. Theory

Methodological problems associated with kinetic analysis of polymer degradation and stability have been well discussed in literature [2]. Both theoretical assumptions and experimental conditions are known to affect the reliability of obtained values for activation energy. In this study, thermogravimetric analysis under multiple heating rates reduces statistical ambiguity associated with the kinetic model assumed. Isoconversional methods, both model-free and integral [2] will be used to assess the computational variation of the calculated activation energies.

### 3. Results and Discussion

Using data from thermogravimetric analysis (TGA), various linearized forms of the kinetic equation can be fit using linear regression. For the model-free method, two approximations [1, 3] are used for the temperature integral.

The forms of integral isoconversional methods are derived from the integrated form of the rate equation. Since this equation does not have an analytical solution, approximations are used on the generalized linear form:

$$\ln\left(\frac{\beta_i}{T_{\alpha,i}^B}\right) = Const - C\left(\frac{E_\alpha}{RT_\alpha}\right)$$

The built-in function *fminsearch()* of MATLAB (version R2010b) is used to locate the minimum function value.

The activation energies calculated at each conversion value are plotted in Figure 1. Initial inspection of the graph indicates that there is a consistent trend showing the variation of activation energy with conversion. The initial mass loss ( $\alpha < 0.20$ )

with higher activation energy is attributed to evaporation of volatile material. In the range of 20-80% degradation, the  $E_a$  values may be considered to vary with minor significance with respect to  $\alpha$ , as the difference between the maximum and minimum within the range is less than 30% of the mean value [4]. This indicates that a single mechanism is followed through the most part of the resin decomposition.

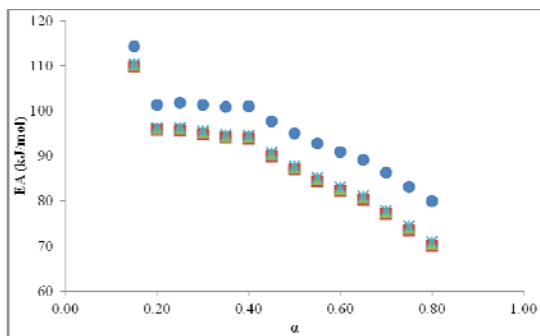


Fig. 1 Variation of E with respect to conversion (○ Flynn-Wall-Ozawa, □ Kissinger-Akahira-Sunose, Δ Starink, × Vyazovkin [Agrawal approx.], \* Vyazovkin [Cai approx.])

Except for the Ozawa-Flynn-Wall method, the choice of temperature integral approximation affects the resulting calculations minimally; based on the results, there is a strong agreement between all the other methods, which suggests that the activation energy for the degradation of furan resin is approximately 88 kJ/mol (Table 1).

Table 1. Determination of Activation Energy

Method	Calculated E (kJ/mol)
Ozawa-Flynn-Wall	95.4178
Kissinger-Akahira-Sunose	87.7722
Starink	88.2044
Vyazovkin (Agrawal approx.)	88.5013
Vyazovkin (Cai approx.)	88.4998

The method of invariant parameters is used to obtain a model-free prediction for the pre-exponential factor. A form based on the Cotes-Redfern method [2] is applied with selected kinetic models of decomposition for the compensation effect [4].

For lifetime prediction, a phase boundary reaction model is expected for the system as the geometry and mechanism of experimentation provides such conditions. Since a single-step process can be assumed for the degradation, the kinetic equation can

be expressed as:

$$t_{\alpha} = \frac{g(\alpha)}{A \exp(-E / RT_0)}$$

to determine the time expected to reach a given conversion at a constant temperature  $T_0$ . Mass loss is taken to be the criteria of degradation, with 5% loss ( $\alpha = 0.05$ ) as the limit for usefulness. The predicted useful life of the resin at different temperature conditions is shown in Figure 2.

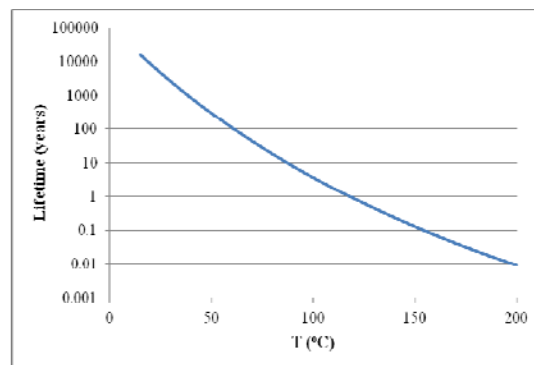


Fig.2 Predicted Useful Lifetime of Synthesized Furan Resin

#### 4. Conclusion

A comparison of Vyazovkin's isoconversional method with integral methods yielded similar values of the activation energy for the decomposition reaction. It is recommended for future work that complete confirmation of the kinetic triplet be concluded by verifying the reaction mechanism. Other optimization methods can also be used on the TGA data to affirm the accuracy of the kinetic triplet. Aside from mass loss as criteria, further study can investigate the relevant physical and chemical properties as functions of the resin degradation to create the full criteria for useful lifetime.

#### References

- [1] R.K. Agrawal, M.S. Sivasubramanian (1987). *AIChE Journal* **33**: 1212-1214.
- [2] P. Budrugaec (2005). *Polymer Degradation and Stability* **89**: 265-273.
- [3] J. Cai, F. Yao, W. Yi, F. He (2006). *AIChE Journal* **52**: 1554-1557.
- [4] S. Vyazovkin, et al. (2011). *Thermochimica Acta* **520**: 1-19.

## Investigation of damage behavior in paper-based friction materials under compressive loading

Naoya URATA, Tomoyuki FUJII, Keiichiro TOHGO and Yoshinobu SHIMAMURA

Department of Mechanical Engineering, Shizuoka University,  
3-5-1 Johoku, Naka-ku, Hamamatu, Shizuoka, 432-8561, Japan  
e-mail: nurata@mechmat.eng.shizuoka.ac.jp

### 1. Introduction

Paper-based friction materials are used for clutch discs of automatic transmission. Performance and reliability of automatic transmission depend on mechanical properties of paper-based friction materials. Cyclic compression tests as conventional tests have been conducted in order to evaluate fatigue strength of paper-based materials. Figure 1 shows the thickness reduction of the paper-based materials composed of aramid fiber or cellulose fiber as a reinforcement as a function of number of cycles from the results of the conventional tests. The tests were conducted under cyclic load with the maximum compressive stress of 60MPa and stress ratio of 0. The thickness of both materials decreases with increasing the number of cycles. The aramid-based and cellulose-based material are broken at around  $10^6$  and  $10^5$  cycles, respectively. The fatigue life of the cellulose-based friction material is shorter than that of aramid based friction material. These fatigue properties are attributed to deformation and damage in internal microstructure, such as fiber and resin. However, the deformation and damage behavior of paper-based friction materials have not been clarified.

This paper deals with the deformation and damage behavior of paper-based friction materials under the cyclic compressive loading. The influence of compressive stresses on damage behavior in internal microstructure was

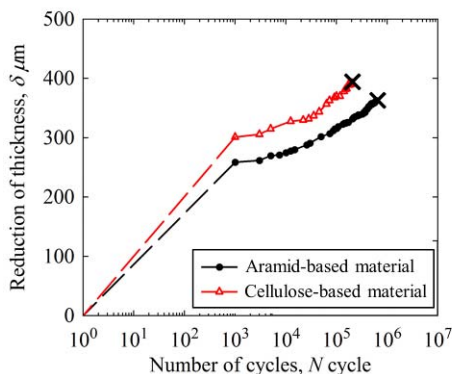


Fig.1 Reduction of thickness conventional compression

test as a function of number of cycles

examined.

### 2.Experiment

#### 2.1 Material and specimen

The materials used are aramid-based and cellulose-based friction materials. The aramid-based and cellulose-based material are composed of aramid fiber and phenolic resin, and cellulose fiber and phenolic resin, respectively. The both materials include the fiber of 70wt% and phenolic resin of 30wt%. The thickness of both materials is  $1.1 \pm 0.1\text{mm}$ .

The materials were cut into square shape with 10mm on a side. Preliminarily, the precise cross-section was formed by the cross-section polishing machine(CP) in order to observe the cross-section by a scanning electron microscope(SEM).

#### 2.2 Cyclic compressive test

The cyclic compressive tests were carried out in order to investigate the influence of compressive stress on the damage behavior in the paper-based friction materials. The tests were carried out under the pure compressive cyclic stress with the stress ratio of 0.1 and applied load rate of 0.1kN/min. The maximum stress increased stepwise up to 100MPa. The compressive cyclic load was repeated five times. After the fifth cycle at same stress level, the cross-section was observed by using SEM and the deformation and damage behavior in microstructure was investigated. Figure 2 shows the observation area on the cross-section of the cellulose-based material. The 12 areas in the cross-section were observed by using SEM. Three specimens were

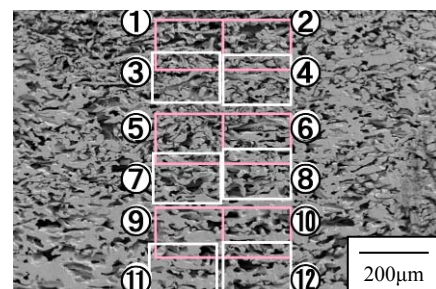


Fig.2 Observation area during compressive test.

prepared for each of materials.

### 3. Results and Discussion

Figure 3 shows the typical cross-section of the aramid-based material during the cyclic compressive test. According to Fig. 3(a), the aramid fibers and pre-existing damage inside of the aramid fiber are observed. When the compressive stress is 20MPa, a crack propagates from the pre-existing damage. When the compressive stress is 50MPa, two aramid fibers move and are crushed. Therefore, it seems that the damage occur inside of aramid fibers.

Figure 4 shows the typical cross-section of the cellulose-based material during the cyclic compressive test. According to Fig. 4(a), the cellulose fibers and resin are observed on the cross-section. It seems that the fibers are glued each other with the resin. When compressive stress is 20MPa, the interfacial debonding between the cellulose fiber and resin occur. When compressive stress is 50MPa, the interfacial debonding occurs in other part. Moreover, the crack initiation is observed inside of the cellulose fiber.

In order to evaluate the damage behavior of the paper-based friction material quantitatively, the damage ratio  $D$  is defined as a ratio of the number of images containing damages and total number of images.

$$D = \frac{\text{Number of images containing damages}}{\text{Total number of images}} \quad (1)$$

Figure 5 shows the damage ratio as a function of compressive stress. For the aramid-based material, when the compressive stress is 10MPa, the initial damage occurs and the damage ratio increases with increasing compressive stress. When compressive stress is 100MPa, the damage ratio is 0.5. For the cellulose-based material, the initial damage occurs under 5MPa and the damage ratio increases with increasing compressive stress, rapidly. When compressive stress is 20MPa, the damage ratio becomes nearly 1.0.

Consequently, the damage in the cellulose-based material occurs under lower compressive stress than in the aramid-based material. Therefore, it seems that the fatigue life of cellulose-based material is shorter than that of aramid-based material.

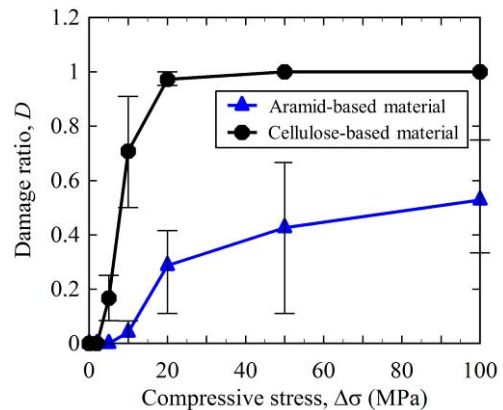
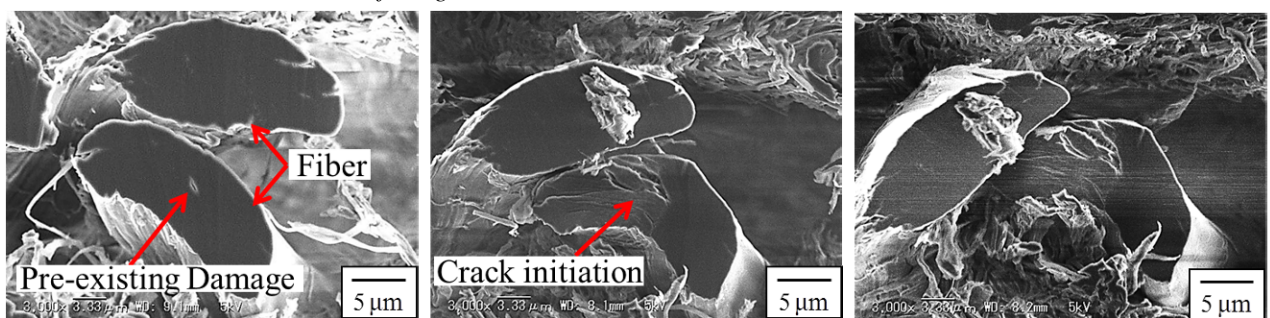


Fig.5 Damage as a function stress level.

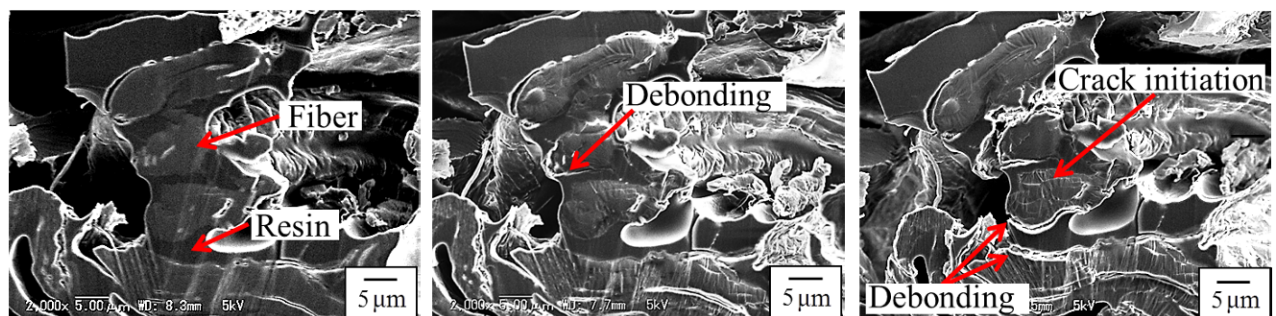


(a) Before test

(b)  $\sigma_{Max} = 20MPa$

(c)  $\sigma_{Max} = 50MPa$

Fig.3 Microstructure during cyclic compression test (Aramid-based material).



(a) Before test

(b)  $\sigma_{Max} = 20MPa$

(c)  $\sigma_{Max} = 50MPa$

Fig.4 Microstructure during cyclic compression test (Cellulose-based material).

## Step-wise Intercalation of Polyetheramine and Paraffin in Montmorillonite

Bryan G. Alamani<sup>\*1</sup>, Rizalinda L. De Leon<sup>1</sup>, Angela D. Escoto<sup>1</sup>, and Jiang Jen Lin<sup>2</sup>

<sup>1</sup>Department of Chemical Engineering, College of Engineering, University of the Philippines Diliman, Philippines

<sup>2</sup>Institute of Polymer Science and Engineering, College of Engineering National Taiwan University, Taipei, Taiwan  
 TEL&FAX: +63-929-6640

\*e-mail: bgalamani@upd.edu.ph

### 1. Introduction

A certain class of organophilic clay modified by Polyoxypropylene Amine as intercalants has been reported. [1-3] [4, 5] These polymers render the layered clay, Montmorillonite in this case, hydrophobic and then lead to increase in the basal spacing from 12Å to 52Å. The mentioned increase has not been observed in the case of surfactants [6] and hydrophilic polymers like polyethylene glycol [7]. The widened gallery spacing will provide more space for materials to be incorporated later on with compatible organic molecules such organic phase change material(PCM). Polyoxypropylene Amines have mono-, di- & tri-amine functionalities that can be reacted with an acid to generate a corresponding quaternary ammonium salt that can interact with the ionic surface of the clay. These molecules, sometimes called Polyether amines, have the capability of tailoring the basal spacing expansion of Layered Silicates such as Montmorillonite (MMT) based on the chain length, molecular weight, number of amine functionalities, presence of other functional groups in the terminal. [1-4, 8-12]

The current study focuses on incorporation of Paraffin (C<sub>18</sub>H<sub>38</sub>) as PCM into the Polyoxypropylene intercalated Layered Montmorillonite without the use of Ionic surfactants and just by allowing common molecular forces brought by intermolecular forces of attraction to incorporate paraffin into the interlayer. Furthermore, the study places emphasis on step-wise intercalation in incorporating organic phase change material in the organophilic layered montmorillonite. The work offers an alternative to the preparation

of clay without the use of surfactants, stabilizers and other compatibilizing materials in order incorporate organic phase change materials.

### 2. Step-wise intercalation of polyoxypropylene amine and paraffin in montmorillonite

The intercalation of Na<sup>+</sup>-MMT performed by ionic exchange reaction with HCl acidified M2000. The procedures for using M2000 as intercalation agent are described below. Sodium montmorillonite (1.00 g, 1.20 mequiv/g) in 100 g deionized water was swelled under mechanical stirring at 80 °C overnight. Acidified M2000 (0.125 g, 35% HCl) was added to the clay slurry at 80 °C for and allowed to react for one hour. 1 to 10 CEC of C<sub>18</sub>H<sub>38</sub> (0.6096 - 6.096 g) was added to the polyoxypropylene amine intercalated clay (MMT/M2000, 1/1 CEC ratio) and the reaction proceeded at temperature of 45 °C with mechanical stirring. The reaction proceeded for 5 hrs and product was collected via vacuum filtration. The final product was washed 2 to 3 times with water and ethanol to remove excess unreacted salts and organic phase change material. The product was dried in the oven at 70 °C for 12 hours.

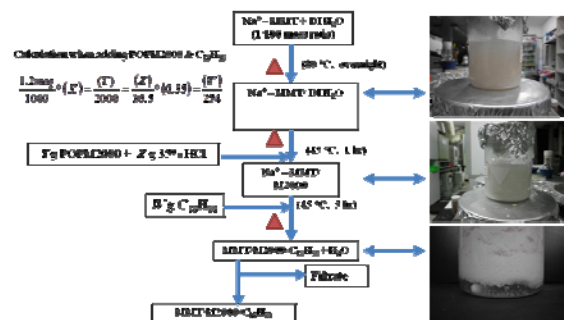


Fig. 1 Schematic of the preparation of the nanocomposites.

### 3. Results and Discussion

Poly(-oxypropylene) monoamine with approximate molecular weight of 2000g/mol or simply M2000 was intercalated in the clay gallery leading to an enlargement of the basal spacing up to 71 Å. Addition of excessive  $C_{18}H_{38}$  led to further expansion of the interlayer which was analyzed via X-ray Diffraction. XRD results revealed an increase in the  $d$  spacing to about 79 to 98 Å. 98 Å was the highest detectable basal spacing value based on XRD which corresponds to 6 CEC of  $C_{18}H_{38}$  added to the organoclay MMT/M2000 (CEC ratio, 1/1) which correspond to a single peak. However, further addition of  $C_{18}H_{38}$  was observed to give relatively featureless XRD profile with some small peak like features. This particular situation tells the need to use transmission electron microscopy (TEM) in order to see the actual basal spacing of the organoclay.

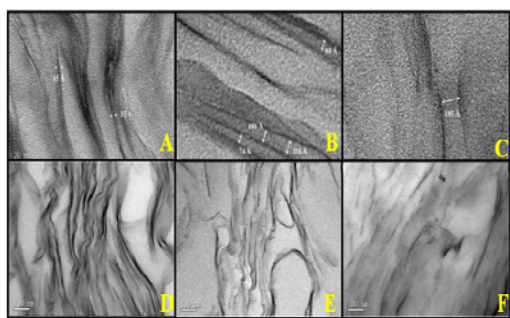


Fig. 2 TEM Images of Phase Change Nanocomposites.

(A) 1/1/6 PHYSICAL MIXTURE (20 nm), (B) 1/1/6 (20 nm), (C) 1/1/10 (20 nm) (D) 1/1/6 PHYSICAL MIXTURE (100 nm), (E) 1/1/6 (100 nm), (F) 1/1/10 (100 nm)

1/1/6 PCN revealed a consistent value of basal spacing with that of XRD (101 Å). 1/1/10 PCN was found out to have a basal spacing of 185 Å which may indicate exfoliation of the clay as this was also consistent with the featureless profile given in the XRD data. For reference, the 1/1/6 physical mixture revealed a basal spacing of 15 Å which was not observed in XRD probably due to large amount of organics thus making the clay morphology undetectable for the said instrument.

Thermogravimetric analysis was used in determining the organic fraction of the composite and it has been found out that the phase change nanocomposites have organic

content essentially similar to that of the composite formulation based on CEC. For example 1/1/6 based on CEC formulation has 83 % organic fraction and thermogravimetric results obtained gave a value of 82 %.

### 4. Conclusion

Nanocomposites were fabricated using step-wise intercalation of polyoxypropylene monoamine and paraffin in montmorillonite. The basal spacing increases as the amount of intercalants increases. The resulting clay morphology was observed to be intercalated and exfoliated depending on the amount of organic incorporated. Thermogravimetric analysis has revealed the high organic fraction for nanocomposites with high basal spacing.

### References

- [1] C.-C. Chou, F.-S. Shieu, J.-J. Lin, *Macromolecules*, 36 (2003) 2187-2189.
- [2] C.-C. Chou, Y.-C. Chang, M.-L. Chiang, J.-J. Lin, *Macromolecules*, 37 (2003) 473-477.
- [3] J.-J. Lin, J.-C. Wei, W.-C. Tsai, *The Journal of Physical Chemistry B*, 111 (2003) 10275-10280.
- [4] J.-J. Lin, Y.-M. Chen, W.-C. Tsai, C.-W. Chiu, *The Journal of Physical Chemistry C*, 112 (2003) 9637-9643.
- [5] S.-T. Lin, C.-W. Chiu, W.-C. Chen, J.-J. Lin, *The Journal of Physical Chemistry C*, 111 (2007) 13016-13021.
- [6] Y. Xi, R.L. Frost, H. He, *Journal of Colloid and Interface Science*, 305 (2007) 150-158.
- [7] M.M. Malwitz, A. Dundigalla, V. Ferreiro, P.D. Butler, M.C. Henk, G. Schmidt, *Physical Chemistry Chemical Physics*, 6 (2004).
- [8] J.-J. Lin, J.-C. Wei, T.-Y. Juang, W.-C. Tsai, *Langmuir*, 23 (2003) 1995-1999.
- [9] J.-J. Lin, Y.-C. Hsu, K.-L. Wei, *Macromolecules*, 40 (2003) 1579-1584.
- [10] J.-J. Lin, Y.-M. Chen, *Langmuir*, 20 (2004) 4261-4264.
- [11] C.-C. Chu, M.-L. Chiang, C.-M. Tsai, J.-J. Lin, *Macromolecules*, 38 (2005) 6240-6243.
- [12] C.-W. Chiu, C.-C. Chu, S.A. Dai, J.-J. Lin, *The Journal of Physical Chemistry C*, 112 (2008) 17940-17944.

## Influence of particle size and debonding damage on elastic and elastic-plastic singular fields around a crack-tip in particulate-reinforced composites

Takahiro OMI, Tomoyuki FUJII, Keiichiro TOHGO<sup>\*3</sup>, Daisuke KATO  
and Yoshinobu SHIMAMURA

Dept. of Mechanical Engineering, Shizuoka Univ.  
Johoku 3-5-1, Naka-ku, Hamamatsu, Shizuoka, 432-8561 Japan

### 1. Introduction

Particulate-reinforced composites have been developed by dispersing particles in matrix in order to improve mechanical performance of materials. In particulate-reinforced composites, it is reported that debonding between matrix and particles or cracking damage of particle affect their mechanical properties. Tohgo et al. developed a constitutive model taking account of particle size effect and damage evolution.

In this paper, a finite element method based on the constitutive model has been developed. Numerical analyses of a crack-tip field under three point bending are carried out for composites containing various sized particles. Influence of debonding damage on stress field ahead of a crack-tip is discussed based on the numerical results.

### 2. Finite element analysis

**2.1 Incremental damage theory** Tohgo et al. developed damage theory of composites taking account of debonding damage evolution based on Eshelby's equivalent inclusion method and Mori-Tanaka's mean field concept<sup>(1)</sup>. The constitutive relation is described by the form decomposed into the hydrostatic and the deviatoric parts as follows:

$$d\varepsilon_{kk} = \frac{1}{3\kappa_t} d\sigma_{kk} + \frac{1}{3\kappa_d} \sigma_{kk}^p df \quad (1)$$

$$d\varepsilon_{ij}' = \frac{1}{2\mu_t} d\sigma_{ij}' + \frac{1}{2\mu_d} \sigma_{ij}'^p df \quad (2)$$

where,  $df$  is the volume fraction of the particles to be debonded in the incremental process  $k_t, k_d, \mu_t$  and  $\mu_d$  are constant values determined by elastic moduli of matrix and particle.

**2.2 Particle size effect** The theory described above is extended to consider the particle size effect by Nan-Clarke's simple method. The stress-strain relation is given by Ramburg-Osgood equation as follows:

$$\varepsilon_e^0 = \frac{\sigma_e^0}{E_0} + \lambda \frac{\sigma_0^0}{E_0} \left( \frac{\sigma_e^0}{\sigma_0^0} \right)^{1/n} \quad (3)$$

where,  $E_0, \sigma_0^0$ , and  $n$  is Young's modulus, yield stress and work-hardening exponent, and  $\lambda$  is a material constant. Nan-Clarke assumed that yield stress was affected by particles, and then modified as follows:

$$\sigma_0^0 = (\sigma_0^0)_{\text{Bulk}} + \Delta\sigma_0^0 \quad (4)$$

where,  $\Delta\sigma_0^0$  is the correction term taking account of the particle size effect and is expressed as a function of particle size  $d$ .

In order to consider the particle size effect on damage, it is assumed that the debonding damage is controlled by a strain energy release rate criterion for particle-matrix interfacial debonding. From energy balance during debonding process of a particle, the critical particle stress for debonding damage is approximately given as follows:

$$\sigma^{cr} = \frac{K_{IC}}{\sqrt{d}} \quad (5)$$

where,  $K_{IC}$  is the fracture toughness for interfacial debonding between the particle and matrix.

**2.3 Particle size distribution** A number distribution of particles is assumed to follow a lognormal distribution.

$$p(d) = \frac{1}{\sqrt{2\pi}\delta d} \exp\left[-\frac{(\ln d - \phi)^2}{2\delta^2}\right] \quad (6)$$

where,  $\delta$  and  $\phi$  is constant. Influence of each particle on macroscopic property of composite described by the volume percentage  $p_v(d)$ . The volume percentage of particle  $p_v(d)$  is given by

$$p_v(d) = \frac{1}{\int d^3 p(d) dd} d^3 p(d) \quad (7)$$

Consequently, some values A, such as the stress and strain, of a composite containing various sized particles can be obtained by the

following equation,

$$A = \int p_v(d)A(d)dd \quad (8)$$

where,  $A(d)$  exhibits the values for a composite with constant sized particles of  $d$ .

**2.4 Analytical condition** Finite element method was formulated on the basis of quadrilateral 8-noded iso-parametric elements with four gauss points. Numerical analysis was carried out for the composite of 15vol%SiC/A356-T4. The material properties of matrix are  $E_0=70\text{GPa}$ ,  $\nu_0=0.33$ ,  $(\sigma_0^0)_{\text{Bulk}}=86\text{MPa}$ ,  $n=0.212$ ,  $\lambda=3/7$ . The material properties of SiC particles are  $E_p=427\text{GPa}$ ,  $\nu_p=0.17$  and a particle volume fraction  $f_{p0}$  is 15%. The mean particle diameters are set as  $\bar{d} = 1\mu\text{m}$ ,  $7.5\mu\text{m}$  and  $16\mu\text{m}$ . Figure 1 shows the three-point bending specimen and its finite element mesh. In order to avoid the numerical problem for crack-tip singularity, a sharp notch with radius of  $0.02\text{mm}$  was regard as a crack. The elastic-plastic fracture mechanics parameter J-integral was calculated by a simple evaluation method using load-displacement relations for each stage of deformation.

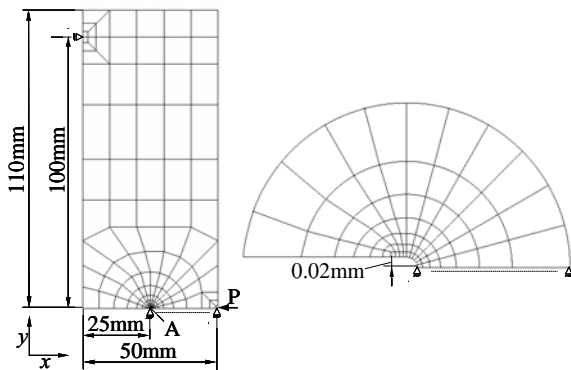


Fig. 1 Dimensions of specimen and its finite elemental meshes

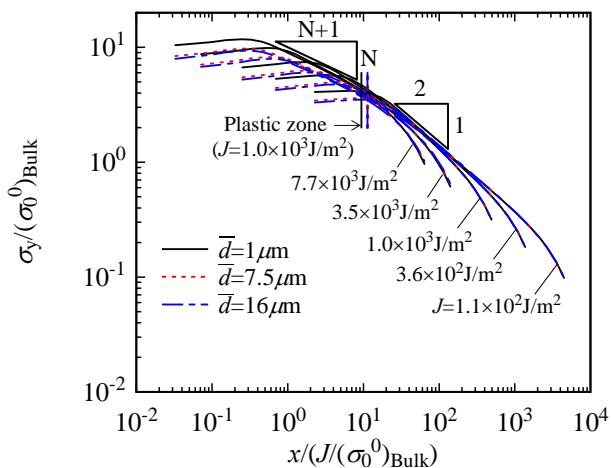


Fig. 2 Distributions of the stress ahead of a crack-tip without debonding damage.

### 3. Analytical results and Discussion

**3.1 Particle size effect** Figure 2 shows the stress distribution at crack-tip taking account of particle size effect. The stress is normalized by  $(\sigma_0^0)_{\text{Bulk}}$  and the distance from crack-tip is normalized by J-integral and  $(\sigma_0^0)_{\text{Bulk}}$ . From a viewpoint of slope of stress distribution, HRR singular field expressed by the straight line with the slope of  $-N/(N+1)$  ( $N$  is work-hardening exponent) is formed in plastic deformation zone near the crack-tip, and  $K$  singular field expressed by a straight line with the slope of  $-1/2$  is formed in elastic deformation zone around the outside of HRR singular field. From a viewpoint of mean particle size, the stress distribution shift upward with decreasing mean particle size, because the yield stress increases with decreasing particle size.

### 3.2 Influence of Debonding damage

Figure 3 shows the normalized stress distribution and void volume fraction distribution at crack-tip in case of mean particle diameter of  $16\mu\text{m}$ . The dotted line denotes the results considering particle size effect(NDD), and the solid line denotes the results considering particle size effect and debonding damage(DD). The stress increases with progressive deformation in the case of no debonding. The debonding initiates from a crack-tip and the stress at the debonding area is lower than that of no debonding in the case of consideration of debonding. The stress reduction around crack-tip is attributed to loss of load carrying capability of particle by debonding between particles and matrix. The area of debonding damage is corresponding to that of stress reduction, and the debonding damage affects the stress reduction around a crack-tip with progressive deformation.

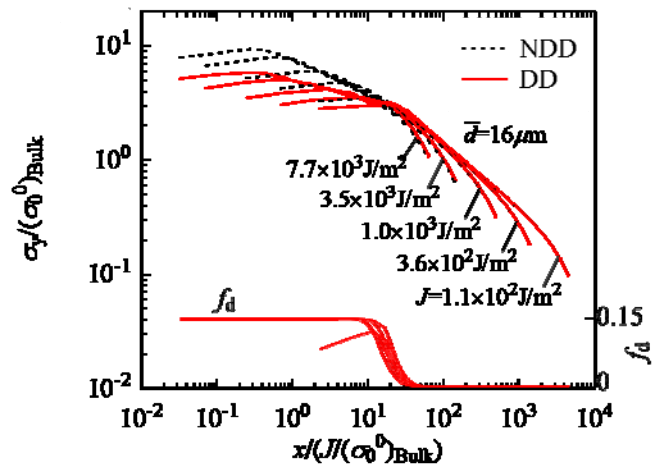


Fig. 3 Influence of debonding damage on distributions of the stress ahead of a crack-tip in the composite of  $\bar{d} = 16\mu\text{m}$ .

## Synthesis and Characterization of Microencapsulated N-Octadecane in Urea-Melamine-Formaldehyde Shell for Thermal Regulation

Dr. Angela Escoto\*, Karl Ezra S. Pilario\*\*, John Gerald S. Reamillo and Noel S. Sabarillo

Department of Chemical Engineering, College of Engineering, University of the Philippines-Diliman,  
1101 Diliman Campus, Quezon City, NCR, Philippines  
Tel. No.: 929-6640

\*Adviser, E-mail: angie\_escoto@yahoo.com

\*\*E-mail: kspilario@gmail.com

### 1. Introduction

Phase change materials (PCMs) have the ability to maintain a steady temperature upon changing phase. These materials are currently used for heat storage and space cooling. This research primarily aims to conduct preliminary observations in the surface cooling of polyurethane foams using PCM technology. Polyurethane foam is the material of construction of car seats and pillows, whose temperatures can reach 60°C-70°C when cars are parked under the sun. A modified microencapsulation technique will be used to synthesize a PCM with n-octadecane and urea-melamine-formaldehyde as core and shell materials respectively. The modified technique is tailored to the availability of reagents and the time and equipment constraints in the Philippines.

The four main objectives of the study are: (1) To develop a modified methodology adapted from Zhang et al for microencapsulation; (2) To synthesize a microencapsulated PCM with n-octadecane as the core material and urea-melamine-formaldehyde (UMF) as the shell material; (3) To characterize the PCM as to its phase change temperature and latent heat of fusion, and; (4) To determine the magnitude of reduction in the temperature profiles of PCM-covered polyurethane foams exposed in a heated environment.

### 2. PCM Synthesis: Microencapsulation by *In Situ* Polymerization

For synthesis, two mixtures were prepared: the pre-polymer solution and the emulsion. The pre-polymer solution contained urea, melamine, and formaldehyde at established proportions, together with distilled water. The emulsion is a

mixture of SDS surfactant, resorcinol, and n-octadecane homogenized for 1.6 hours. The two were then mixed and homogenized at 4400 rpm, including pH regulation to control polymerization. Microencapsulation is done after 2 hours, and samples were taken from different layers in the mixture. They must, then, be filtered from unencapsulated core and excess shell materials. After vacuum filtration, the samples must be dried for 8-10 hours in a gravity oven. Figure 1 shows the final product prior to characterization.



Fig. 1 Microencapsulated PCM prior to Characterization

### 3. Differential Scanning Calorimetry & Temperature Profiling

Characterization is of two parts: Differential Scanning Calorimetry with calibration and temperature profiling using a Data Logger. The generated thermograms were plots of heat flux against the temperature of a sample. Inside the DSC, the sample was heated and cooled for two cycles—determining cycling stability. Phase change temperatures and latent heats were identified through TA Instruments Operating Software integrated into the DSC.

After choosing the best sample, temperature profiling was started by creating a 1 x 1 x 2 ft wooden box with a bulb on its hinged lid as heat source. The best sample was used to completely cover the top surface of foam manually. Together with the control/blank foam and a pure PCM sample, the covered foam was subjected to heating and cooling. Temperature probes were provided for each, as well as the ambient temperature. Hydra Data Logger tabulated and profiled the temperatures for a period of 1.5 hours.

#### 4. Results and Discussion

Figure 2 shows the thermogram of the best sample where the heating cycle is analyzed. The generated peak melting temperature is 1.6°C lower, and the latent heat of fusion is 23.8 J/g higher compared to the results obtained in the original study by Zhang et al. This implies that the modified methodology yielded microencapsulated products with better thermal properties, since a lower peak temperature and higher latent heat of fusion would result to a more appealing environment for human comfort.

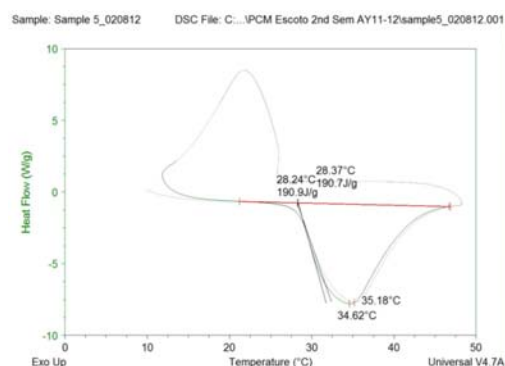


Fig. 2 Thermogram of the sample with the highest latent heat and favorable melting point

From the preliminary observations conducted to compare the temperature responses of the microencapsulated product and polyurethane foam when exposed under the same heating conditions, it was observed that the temperature of the product was lower by an average of 3.56°C relative to the blank polyurethane foam sample, and by an average of 1°C relative to the ambient temperature. The

temperature profiles of the materials during heating are presented on Figure 3.

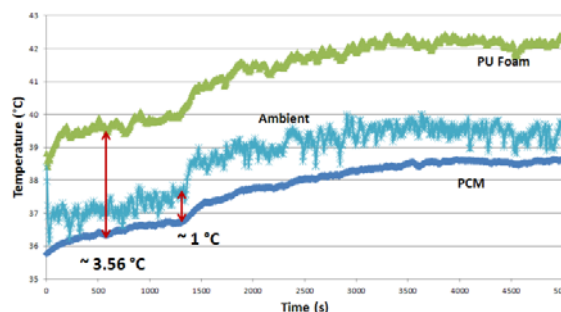


Fig. 3 Temperature profile of the PCM, foam, and ambient temperature during heating

#### 5. Conclusion

Based from ocular observations and the results of the DSC characterization, n-octadecane was successfully microencapsulated in urea-melamine-formaldehyde shell. The best microcapsule samples had a peak melting temperature of 34.9°C and a latent heat of fusion of 190.8 J/g. From the preliminary observations done in temperature profiling, the product is thermally feasible for polyurethane foam applications, like in car pillows and car seats.

#### 6. References

- [1] Alkan, C., Sari, A., and Karaipekli, A. 2010. Preparation, thermal properties and thermal reliability of microencapsulated n-octadecane as novel phase change material for thermal energy storage. *Energy Conversion and Management* 52 (2011) 687–692
- [2] Mehling, H. and L. F. Cabeza. 2008. *Heat and Cold Storage with PCM: An up to date introduction into basics and applications.* Springer-Verlag Berlin Heidelberg, Germany.
- [3] Zhang, X., Fan, Y., Tao, X., & Yick, K. (2004). Fabrication and properties of microcapsules and nanocapsules containing n-octadecane. *Materials Chemistry and Physics*, 300–307.